Materials Advances

REVIEW

View Article Online
View Journal | View Issue

Cite this: *Mater. Adv.*, 2025, **6**, 3386

Bridging current and future innovations to unlock the potential of multifunctional materials for sustainable energy applications

Aparna Ashok,[a] Jitendra Pal Singh,[b] Anuj Kumar[c] and Neeru Bhagat*[d]

Received 6th February 2025,
Accepted 28th April 2025

DOI: 10.1039/d5ma00102a

rsc.li/materials-advances

The growing demand for clean and reliable energy is pushing researchers to explore a wide variety of advanced materials for energy applications. These materials are at the heart of many technologies that aim to produce, store, and use energy more efficiently and sustainably. Today, energy materials are being developed for a broad range of applications, including solar cells (photovoltaics), thermoelectric devices, batteries, fuel cells, and supercapacitors. Each of these technologies requires materials with specific properties, and finding or designing such materials presents exciting opportunities and complex challenges. For instance, high-performance battery materials are essential for grid-scale energy storage systems, which are needed to balance the supply of and demand for electricity, especially when using renewable sources such as solar and wind energy. In fuel cells, materials must support fast ion transport and be chemically stable over long periods. Similarly, in carbon capture systems, materials must effectively absorb and store carbon dioxide to help reduce greenhouse gas emissions. These diverse requirements have led the scientific community to search for new materials with enhanced properties, such as higher conductivity, better thermal stability, and improved mechanical strength. Recently, the use of machine learning (ML) and nature-inspired optimization (NIO) has started to transform how materials are discovered and optimized. Instead of relying only on trial-and-error experiments, researchers can now use AI tools to predict which materials might perform well in specific energy applications. This significantly speeds up the development process and helps design materials with customized features. Overall, this review highlights a wide selection of current and next-generation materials, along with the role of machine learning in shaping the future of sustainable energy. Together, these advancements hold great promise for addressing global energy challenges and building a cleaner, more efficient energy landscape.

1 Introduction

Energy materials encompass a broad spectrum of materials tailored to meet the demands of diverse energy applications by optimizing energy performance[1–11] through high-throughput machine learning,[2] comparing and categorizing storage types,[3] and improving the figure of merit[4] for building next-generation solution-processed, high-performance and low-cost opto-electronic devices,[5] phase-transformation-based energy conversion,[6] entropy effect and formation enthalpy for storage,[7] emergence of carbon and graphene-based materials as energy devices,[8] efficient materials that have higher capacitive retention and obey charge transfer resistance,[9] power generation and cooling or heating applications[10] and developing stable catalysts for accelerating reactions involved in energy conversion and storage processes.[12] At the forefront of this field are materials designed for energy conversion,[13] storage,[14] and transmission,[15] with each of them playing a pivotal role in transitioning towards sustainable energy. The core concept in energy-material research is the quest for materials with enhanced performance and durability. These materials have a wide range of compositions, structures, and functionalities. Energy material research encompasses diverse materials and technologies critical for addressing global energy challenges.[16,17] The interdisciplinary nature of this research covers the fundamental principles of physics, the nuanced complexities of materials science, and the transformative potential of nanotechnology.

---

[a] Department of Applied Science, Symbiosis Institute of Technology, Symbiosis International (Deemed) University, Pune, Maharashtra-412115, India
[b] Department of Sciences, Manav Rachna University, Faridabad, Haryana-121004, India
[c] School of Computer Science Engineering and Applications, D.Y.Patil International University, Pune, Maharashtra-411044, India
[d] St. Mira's College for Girls, Koregaon Road, Pune, Maharashtra-411001, India. E-mail: neerubhagat@hotmail.com

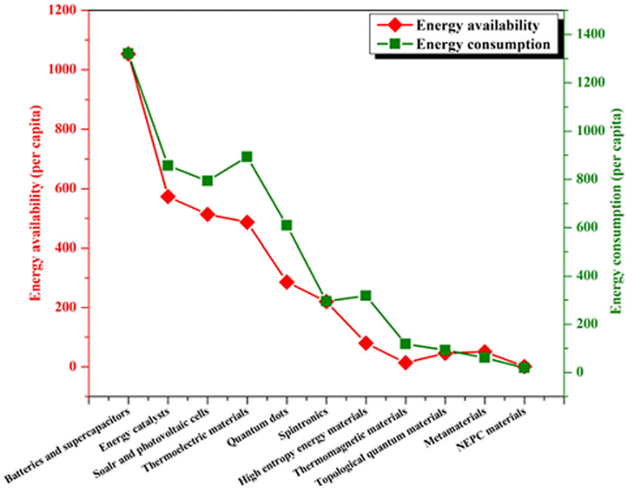

Fig. 1 Trends in different kinds of energy materials.

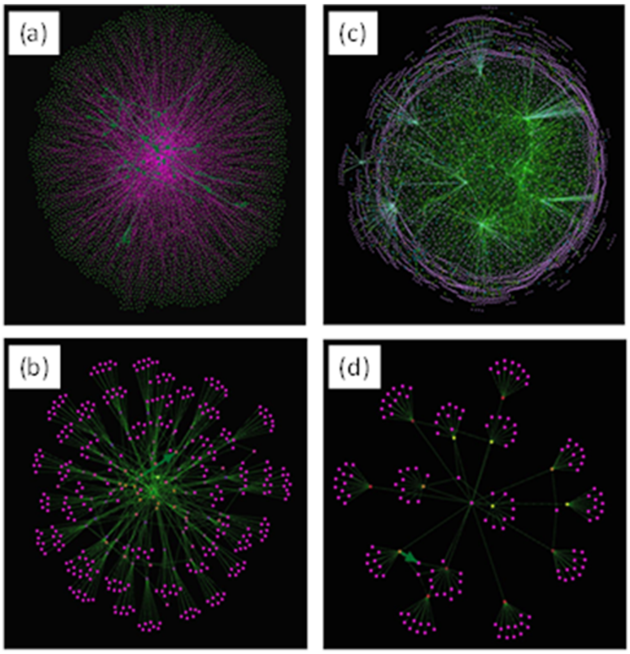

Fig. 2 Network visualizations of the impact of energy materials drawn from layout algorithms accessible in Gephi. (a) Energy sector data drawn from the nodes for different applications using the Fruchterman Reingold algorithm. (b) Detection of cohesive groups using the Yifanhu proportional algorithm. (c) Clusters describe the renewable energy resources derived from the force atlas algorithm. (d) Network connectivity envisaged from the force atlas algorithm using energy data obtained from renewable energy and Heusler alloys.

In the energy sector, materials such as Heusler alloys, high-entropy energy materials, magnetocaloric materials, half-metallic ferromagnets, topological quantum materials, thermoelectric generators, spintronics, metamaterials, energy catalysts, supercapacitors, solar cells, nanomaterials, nano-enhanced phase change materials, and quantum dots play a crucial role in energy consumption and production. The energy materials trend regarding energy availability and consumption based on the materials discussed in this review is shown in Fig. 1.

Batteries and supercapacitor-based materials consume most of the energy available from renewable and non-renewable sources, and their consumption is greater than the supply. To develop high-quality and well-developed batteries and supercapacitors, the use of materials is in high demand, and hence, the consumption is more than the production. The thermoelectric, solar, and photovoltaic cells closely follow, with the yield being significantly less in terms of the overuse of energy materials. This trend indicates a high chance of waste of materials in the development of devices, as consumerism dominates overproduction. The trend is lower regarding metamaterials, high-entropy materials, topological quantum materials, quantum dots, and nano-enhanced phase-changing (NEPC) materials due to their research being at an early stage and lesser demand in the global energy challenges.[18–21] However, the consumption is still higher than the availability because of the depletion of materials and the dwindling of resources. As intermittent renewable energy sources become a more significant part of India's energy mix, there will be an increased demand for energy storage solutions to ensure grid stability and reliability. Advanced materials for high-efficiency transformers, conductors, and power electronics will play a vital role. India's industrial sector is expected to grow, driving demand for materials that enable cleaner and more sustainable manufacturing processes. This includes catalysts, membranes, and materials for carbon capture, utilization, and storage (CCUS) technologies.

Material science plays an imperative role in transitioning energy to a sustainable form. Although accidental discoveries remain one of the cradles for new materials, the traditional pragmatic approach of the ''trial-and-error'' method of innovation has been augmented by the era of machine learning and optimization for the unearthing of novel materials. A profound understanding of the basic physics and chemistry of materials is mandatory, and along with this, the capability to measure and fabricate materials at the molecular and nanoscale level brings out the freshness in the engineering of materials for energy applications.[3,22,23] The visualization of the impact of energy materials in the research conducted in India based on renewable energy sources was performed using the open-source software Gephi, which could facilitate filtering, navigation, manipulation, and clustering of network data. Energy resources have been categorized in an enormous dataset where renewable energy materials are clustered in terms of network structures. The cluster density (marked in pink colour) is shown in Fig. 2a. It denotes the amount of research happening in the sector of renewable energy resources. The nodes represent solar cells, photovoltaic, batteries, and supercapacitors, which are applications. Edges relate to Heusler alloys, metamaterials, high-entropy energy materials, topological quantum materials, thermoelectric and magnetic materials, quantum dots, and nano-enhanced phase-changing (NEPC) materials. The visualization was implemented using the Fruchterman Reingold algorithm, which is a complete network web consisting of all the segments discussed in the review. Fig. 2b shows the community detection in the visualization performed using the Yifanhu proportional algorithm. The structure formed here can be utilized to uncover cohesive groups (depicted in green color) with the interjection points representing the Heusler alloys connecting with the application of spintronic, half-metallicity, topological insulators, and thermoelectric generators. Fig. 2c shows the centrality measures of each node in the network to find hubs or significant entities. Based on the connectivity patterns, centrality measures quantify the influence of a node. The entities are represented as green branches, and hubs are represented as pink circles rotating around the renewable materials of energy sources. Fig. 2d shows temporal data and examines how network connectivity and structure change over time. Gephi's force atlas algorithm was used to examine patterns, developments, and new constellations formed in solar energy, batteries, supercapacitors, renewable energy, and Heusler alloys. Not all applications can benefit from proximity between patterns based on distance. The reduction of dimensionality would result from this. The pattern of events was compared using the pattern-based closeness factor. It depicts a coherence and thematic link between one or more items.

Most research on the bulk material requirements of renewable energy systems occurs within life-cycle assessments. These studies offer insightful information about the material requirements of conventional and renewable energy technologies at the unit level. However, they do not offer a holistic view of the bulk material requirements of future advancements in the power sector. Research that estimates bulk material requirements for current scenarios or incorporates bulk material or life-cycle assessments into modelling for the energy sector is uncommon. Here, the materials discussed will be the next generation of power grid materials that could drastically reduce power and energy consumption globally and in the Indian energy sector if these materials are fabricated and devised according to the needs of the government, population, growth, and urbanization.[24,25]

2 Energy conversion materials

2.1 Solar materials

Converting sunlight to electric energy, widely known as solar cell application, is the subject of the most active research into energy conservation and is recognized as a sustainable solution. To date, the most promising materials for this purpose are ternary Cu-based chalcopyrite semiconductors such as p-type $CuInSe_2$ and $Cu/InGaSe_2$.[26–28] This material is known as an affordable light-absorbing material for these applications. In designing devices for solar applications, a buffer layer of CdS, approximately 50 nm thick, is positioned between the n-type ZnO window layer and the light absorber in classic chalcopyrite solar cells to improve performance. The $ZnO/CdS/Cu(In,Ga)Se_2$ heterojunction solar cell has an efficiency of 19.9%. To prevent the barrier from weakening at the interface, the buffer layer must have an inverted-interface combination band of the light absorber material close to the Fermi energy.[21,29–37] This is a key requirement for minimizing recombination.

The key objective of solar cell design is to reduce electron loss during transport and augment the active layer's optical absorption. The performance of solar cells can be enhanced using nanostructures. For example, quantum dots can generate multiple excitons (electron–hole pairs) from a single photon, thereby boosting the efficiency. They also have a large surface area, similar to the nanocrystalline films used in dye-sensitized solar cells, which allows for better light absorption. Nanostructures also produce useful optical effects, such as surface plasmon resonance and light scattering, which help control how much light is absorbed. Additionally, using one-dimensional nanostructures or custom-designed 3D shapes, such as hollow core–shell spheres, can make it easier for electrons to move through the solar cell, improving its efficiency.[38,39]

Quantum dots (QD) are semiconducting materials that exhibit quantum mechanical properties. The reason for integrating quantum dots into solar cells is their increased efficiency and cell performance. The synthesized CdSe quantum dots in various sizes can be used as an inorganic dye to sensitize wide bandgap TiO_2 thin films for QDs solar cells. CdSe quantum dots with diameters between 3 and 6 nm can regulate the optical characteristics and, in turn, enhance the performance of the solar cell.[40–42] A solar cell with a performance of 0.08% under solar radiation with an absolute 100 mW cm^{-2} of light had been achieved at the early stages. The high quantum yield and configurable bandgap of CdSe quantum dots make them promising materials for solar cell applications. They are appropriate for widening the absorption spectrum of solar cells for absorbing a particular wavelength of light.[43] On the other hand, PbS quantum dots with their narrow bandgap are well known for their effective absorption of infrared light. By extending the absorption range of solar cells, particularly in the near-infrared spectrum, quantum dots help solar cells absorb more light.[44] High-performance $TiO_2/CuInS_2$-QDs/CdS/ZnS photoanode quantum dots sensitized solar cells in the presence of polysulfide electrolytes are in demand due to their conversion efficiency. Under a single solar illumination, they obtained an open-circuit photovoltaic (V_{oc}) of 0.56 V, a fill factor of 0.45, a short-circuit photocurrent (J_{sc}) of 16.9 mA cm^{-2}, and a conversion efficiency of 4.2%.[45] ZnO has been used to date as a potential electron-transport layer (ETL) in thin-film photovoltaics. An innovative method for processing pure ZnO at low temperatures for planar heterojunctions using ZnO quantum dots (QDs) is supported by readily removable solvent molecules such as dimethyl sulfoxide. The higher uniformity of the surface morphology and lower defect density of films based on organometallic-derived QDs are attributed to their improved photovoltaic performance. These factors likely ensure enhanced stability of the ZnO/perovskite interface with a maximum power conversion efficiency of 20.05%.[45,46]

To address the challenge with electron–hole pair recombination in TiO_2 conventional solar cells, an ultra-thin layer of MgO is applied. Researchers have methodically investigated the role of each layer of the MgO interface created at the triple junction. A deeper comprehension of the charge recombination mechanisms in these types of cells is vital to achieving higher conversion efficiencies; this will essentially result in novel strategies for blocking the losses due to the recombination of pairs, as mentioned above. Thus, recombination rates notably decreased, and the cell efficiency increased by more than 20%.[47,48]

Colloidal QDs of InP and InZnP show promise as materials for light-emitting devices due to their adequate bandgap, high absorption coefficient, and high bulk carrier mobility. Numerous studies have shown that it is possible to design the structure of metal nanoparticles (NPs) in optoelectronic devices to maximize scattering and minimize absorption across the relevant wavelength range. For instance, Au nanoparticles (AuNPs) were placed on the surface of silicon (Si) p–n photodiodes, and scattering from surface plasmon resonance (SPR) increased optical absorption and photocurrent. Size-controlled Ag nanoparticles (AgNPs) were used to fabricate optically thin GaAs solar cells. Strong scattering by interacting surface plasmons in high aspect-ratio AgNPs caused an 8% increase in the photocurrent of the solar cells.[49] Regarding PV cells (PVCs), in general, these devices have little flexibility and are brittle in their typical designs. Therefore, their projected usage in wearable applications in industries like textiles appears difficult. Applying 1D polymer solar cells in coaxial arrangements onto optical fibers closely followed this breakthrough. Coaxial structures have been used to implement 1D materials for energy harvesting. Excellent photovoltaic qualities are exhibited by polymorphic core/multishell nanowires (NWs), which improve absorption in many solar spectrum regions and pave the way for the creation of ultrathin solar cells of the future.[43,44] The photoelectric properties of the resulting InZnP@PbS–I CQD films, shown in Fig. 3a, are the devices used for measuring the *I*–*t* curves. Here, 405 nm chopped light (about 15 mW cm^{-2}) was used to excite the InZnP@PbS–I CQD films, and the collected data are plotted in Fig. 3b.

Relatively stable *I*–*t* curves of the CQD films without encapsulation at room temperature were observed, indicating that InZnP@PbS–I CQDs are stable photoelectric materials. The photocurrents increased with increasing applied bias voltage. Fig. 3c shows the variation of photocurrent with different bias voltages.

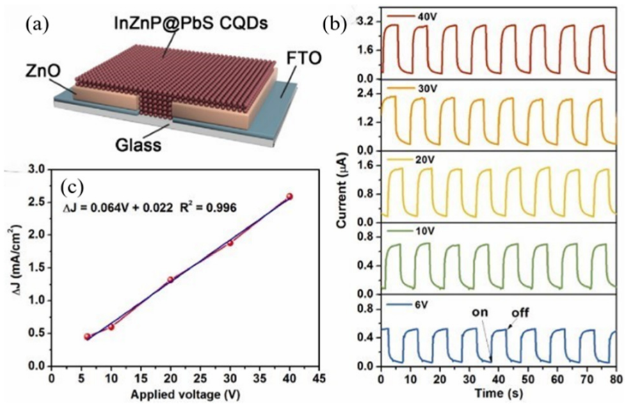

Fig. 3 (a) Schematic diagram of the devices used for collecting *I*–*t* data. (b) *I*–*t* curves of the InZnP@PbS–I CQD films under different bias voltages. (c) Photocurrent density variation with the applied voltage. Reproduced with permission.[5]

Fig. 4a shows the cross-sectional transmission electron microscopy (TEM) image of the constructed solar cell devices possessing the FTO/ZnO/InZnP@PbS–I CQDs/PbS-EDT/MoOx/Ag structure. The related *J*–*V* curves are plotted in Fig. 4b. Fig. 4c shows the electrochemical impedance spectroscopy (EIS) curves of the InZnP@PbS–I CQD-based solar cells (the equivalent circuit was illustrated as an inset). Fig. 15d shows the variation of the solar cell devices' V_{oc}, J_{sc}, FF, and PCE (200 mg mL^{-1} CQD-based sample). After 8 days, no obvious decrease was observed. After approximately 90 days, approximately 87% of the initial PCE can be maintained. Fig. 4e shows the performance comparison of the indium phosphide CQD-based solar cells.[5]

2.2 Thermoelectric materials

While solar cells are being extensively researched, other materials are also being investigated as sources for different energy conversion. Some of these materials are thermoelectric (TE). The temperature dependence of *ZT* for several typical Cu-based diamond-like TE compounds is illustrated in Fig. 5a, where *ZT* is the dimensionless figure of merit for thermoelectric materials. The temperature-dependent lattice thermal conductivity (κ_{L}) of state-of-the-art Cu-based thermoelectric materials is shown in Fig. 5b. The timeline of the figure of merit (*ZT*) of certain Cu-based thermoelectric materials like superionic conductors, tetrahedrites, oxyselenides, and diamond-like compounds is represented in Fig. 5c.[50]

LiZnZ semiconductors, where Z = P, As, or Sb, have bandgap values of ∼2.3, 1.8, and 1 eV, respectively. Theoretical and experimental research was conducted on the electrical structure.[32–35] The observations of direct current transport demonstrate that the conductivity increases with temperature. Even when the electrical conductivity increased when the phosphorous cation was substituted with antimony. High-inclusive efficiency thermoelectric cells (TECs) help reduce the need for fossil fuels by directly converting heat energy into electricity and preventing global warming.[36,37,51–55] A significant advancement in the efficiency of thermoelectric materials could significantly impact the development of sustainable and environmentally friendly energy systems. Due to their costly initial components (Te, Ge, *etc.*) and reported low-efficiency values between 5% and 10%, modern converters are too inefficient to be economically viable. The performance of the materials is given by the figure of merit *ZT* where $ZT = \sigma S_2 \kappa T$, σ = electrical conductivity, S = Seebeck coefficient and κ = thermal conductivity.[56–60] Due to the important electric and thermal connections, the *ZT* loses the most when moving from the raw material to the TE module. Developing TE modules that can operate at operational temperatures requires a basic understanding of phase separation and diffusion in TE materials.[61–63] While processing these modules, loss of *ZT* occurs through the thermoelectric contacts. To overcome these limitations, a rich

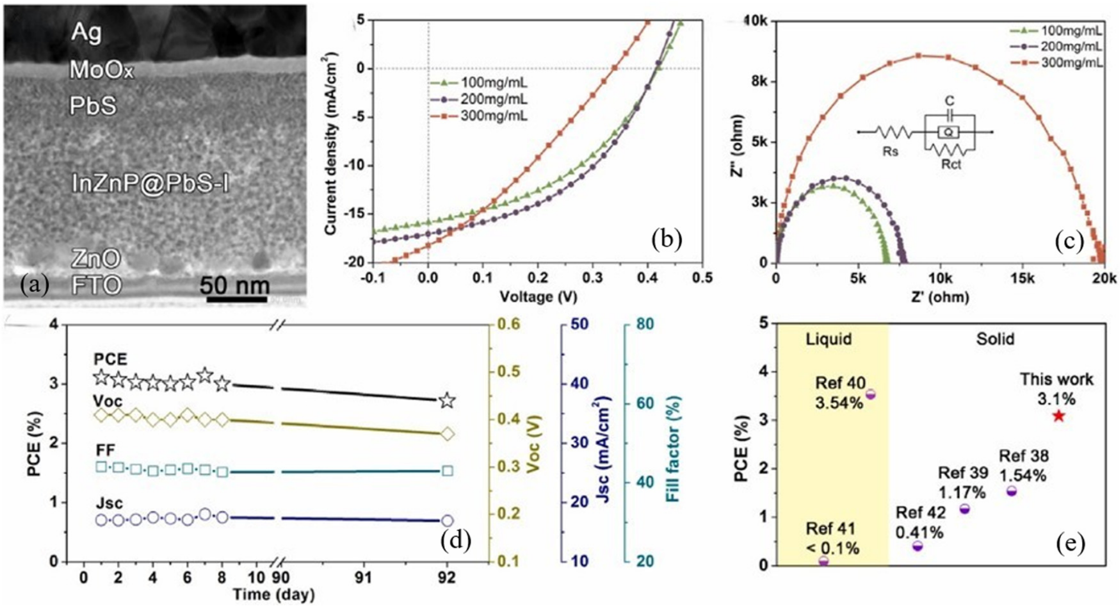

Fig. 4 (a) Cross-sectional TEM image, (b) J–V curves, (c) EIS curves, (d) stability curves of the fabricated InZnP@PbS–I CQD-based all solid-state solar cell devices, and (e) performance comparison of the indium phosphide CQD-based solar cells. Reproduced with permission.[5] Copyright 2024, Elsevier.

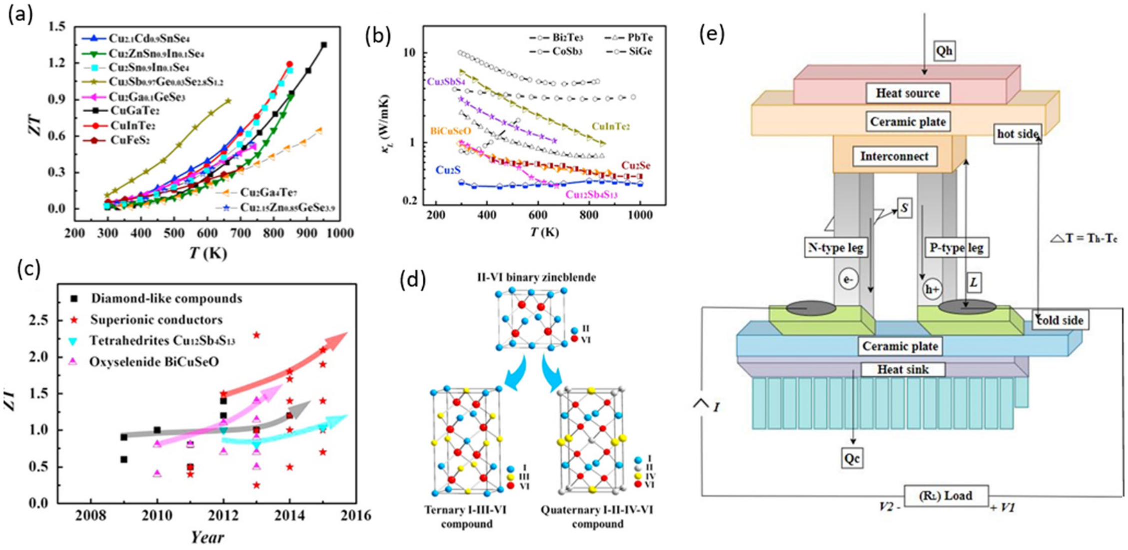

Fig. 5 (a) Crystal structures of diamond-like compounds derived from II–VI binary zinc blende (ZnSe). (b)Temperature dependence of ZT for several typical Cu-based diamond-like TE compounds. Reproduced with permission. (c) Temperature dependence of κ_L for Cu-based state-of-the-art TE materials. (d) Timeline of ZTs in typical Cu-based TE materials. Reproduced with permission.[50] Copyright 2016, Elsevier. (e) Schematic of a thermoelectric generator.

class of half-Heusler semiconductors with 18 valence electrons concentration attracts great attention.[31,64] Heusler compounds, particularly the half-Heuslers, appear to fulfill this role because of their crystalline structure's loose packing, strikingly comparable to that of chalcopyrites.[21,29–31] If the lattice constants of the two materials are within the same range, a satisfactory contact between the surfaces can be obtained. The band gap of the buffer materials, with a lattice constant value of around 5.9 Å, must not be less than 2 eV to ensure a suitably minimal absorption loss. The crystal structures of ternary and quaternary diamond-like compounds derived from II–VI binary zinc blende (ZnSe) are shown in Fig. 5d.

The role of Heusler alloys in energy harvesting has become a focus of interest.[65,66] These compounds are characterized by their specific crystalline structures and tunable compositions, demonstrating their remarkable adaptability in converting various forms of energy to functional power.[67,68] This article comprehensively explores Heusler alloys as thermoelectric materials, elucidating their ability to efficiently harness waste heat and transform it into electrical energy. The intermediate bandgap structure and multifunctional tunability make them formidable contenders for the development of proficient sustainable thermoelectric solutions.[69–71] The capacity for reversible temperature changes in response to magnetic fields can be harnessed for magnetic refrigeration, which is an environmentally friendly alternative to cooling technologies. The role of Heusler alloys as shape memory materials in energy harvesting is also worth mentioning, as they can undergo shape changes under external stimuli, such as temperature fluctuations. This opens new frontiers for developing innovative energy conversion devices with shape memory functionalities.

This makes the research focus primarily on p-type CoTiSb and n-type NiTiSn materials. A power factor of 70 μW (cm K^2)$^{-1}$ at 650 K was obtained for Sb-doped NiTiSn, a celebrated half-Heusler shape memory alloy (SMA).[72–74]

Heat control is another essential component of energy technology. Heat energy can be directly converted into electrical energy using thermoelectric materials (Seebeck effect) or *vice versa* (Peltier effect). They are typically semiconductors with favourable thermoelectric performance (Fig. 5e). Waste heat recovery thermoelectric generators, portable power sources, and energy-efficient cooling/heating systems all require these materials. Radiative cooling appliances generally use photonic crystals with a periodic structure, which creates a photonic band gap that promotes heat dissipation by emitting thermal radiation.[75–77] Graphene and carbon nanotubes with high thermal conductivity can be integrated into a composite and are advantageous materials for heat sinks and thermal interfaces. Certain materials are being used to design thermal barrier coatings that can insulate surfaces from heat and are applied to components in gas turbines and other high-temperature environments, such as aerospace and power generation. Ferroelectric materials display spontaneous electric polarization that is affected by temperature variations. Temperature fluctuations produce electric polarization changes that can be used for power generation in pyroelectric energy harvesting. Nanofluids, a class of heat transfer fluids, have garnered significant attention for their promising applications in cooling systems. These fluids are engineered by suspending nanometre-sized particles, typically metallic or oxide nanoparticles, in a base fluid, often water or other common coolants.[54] Introducing nanoparticles into a fluid alters its thermal properties, enhancing its thermal conductivity and contributing to improved operational efficiency and reduced energy consumption in industrial processes. To control and convert electricity in power systems, motor drivers, inverters, and converters, there is a need for semiconductors with a higher bandgap to boost the input of ideal power electronics. The foremost challenge lies in growing high-quality materials and junction diodes with a large surface area. In high-power switching applications, diamond is the most sought-after material due to its intrinsic qualities like extraordinarily high thermal conductivity, wider bandgap, and high breakdown voltage, which provide a path for insulated-gate bipolar transistors used in high-power switching applications.[78–80]

2.3 Thermomagnetic materials

Heusler alloys-based heat engines with different possible implementations were integrated with small-scale alloy-based heat engines with different possible implementations integrated with small-scale phase transitioning materials that could trigger mechanical vibrations and rotations from a temperature gradient. Thermally activated phase transitions are generally obtained through gas–liquid transition.[81–86] The structural phase transformation, for instance, at a small-scale representative of shape memory alloys, lies in using the ferromagnetic transition of magnetic materials since the associated solid-state conversion permits significant integration potentials.[87–92] Ferromagnetic shape memory alloy (FSMA) materials exhibit the intriguing ability to combine shape memory effects with ferromagnetic properties, leading to innovative concepts in various technological domains. Converting mechanical vibrations or deformations into electrical energy is a well-known use of Heusler alloys as shape memory alloys for energy harvesting.[67,92] The crystal structure of a Heusler alloy with shape memory capabilities changes phase upon mechanical deformation, releasing the stored strain. Depending on the particular design of the energy-harvesting system, the released energy can be captured and converted into electrical power using a variety of techniques, including piezoelectric transduction and electromagnetic induction. Their potential was demonstrated in the field of thermoelectric generators (TEGs), as shown in Fig. 5e. Reports have suggested that concepts involving FSMAs have power densities comparable to those of conventional TEGs.[93–95] This indicates that it can be harnessed as a striding path to harvest waste heat and convert it into consumable electrical power. The dual functionality of FSMAs in shape memory and ferromagnetic behavior contributes to their performance and versatility, thereby providing better applications by upscaling from laboratory-based demonstrations to industrial practice. This scalability factor highlights the adaptability of FSMAs for diverse energy harvesting scenarios. The alloy's chemical composition and the corresponding electron concentration per atomic unit (e/a-ratio), which encourages tailoring over a broad range, significantly influence the transition temperatures, as shown in Fig. 6.[96–98]

Due to inertia, mass and heat upscaling, the performance of the TM generator can be severely affected. This problem can be controlled by maintaining the conditions of resonant self-actuation and rapid heat transfer. The process of manufacturing a TM generator relies basically on cantilever motion, geometry optimization, heat intake, electrical load resistance, and dissipation of thermal radiation between the source and contact of the permanent magnet. Future developments in the field will mostly be driven by the improvement of material properties like thermal conductivity and temperature-dependent magnetization, as well as the development of fabrication technology (*e.g.*, increasing the number of coil turns at the micrometer scale, extending the maximum film thickness). The magnetic behavior of a material, which diminishes with temperature because of a single second-order ferromagnetic transition or the presence of an austenite phase only at low temperatures, is one of the main disadvantages of the current generation of

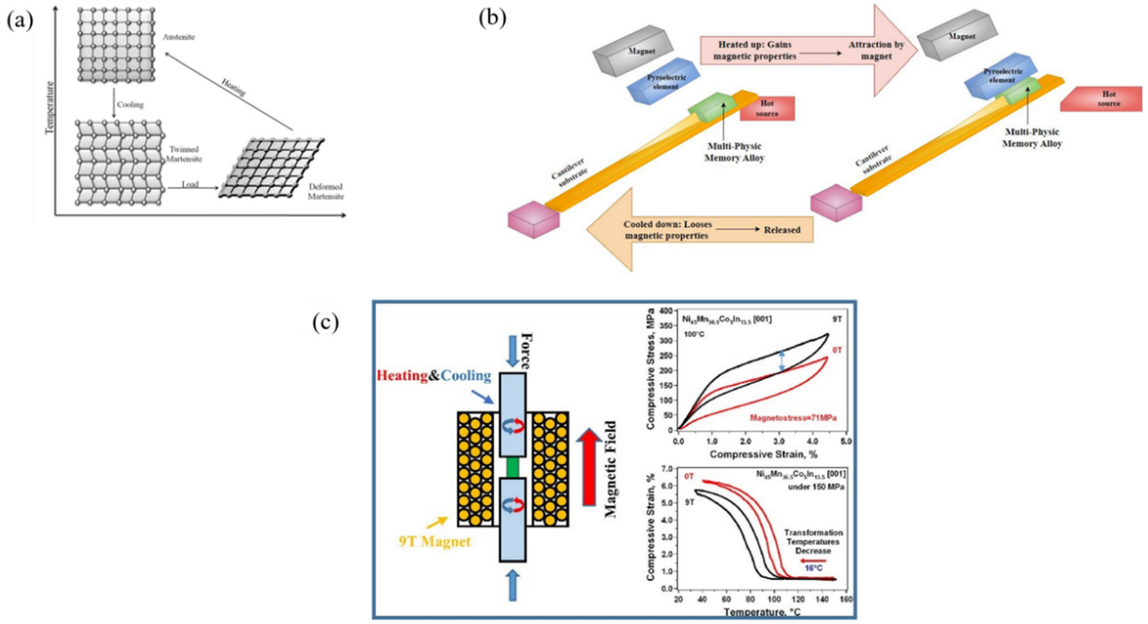

Fig. 6 (a) Diagrammatic representation of the shape memory effect. (b) Heat engine model prototype designed through multi-physics memory alloy (MPMA). (c) Superelastic behavior of [001]-oriented NiMnCoIn single crystals under selected magnetic fields the thermal cycling under 150 MPa and at selected magnetic fields of [001]-oriented NiMnCoIn single crystals. Reproduced with permission,[6] Copyright 2016, Elsevier.

ferromagnetic and FSMA heat engines, in particular, is described in Fig. 6a. This means that to enable mechanical displacement, magnetizing elements (such magnets) must be placed close to the heat source. A more direct energy conversion approach involving direct heat transfer and subsequent conversion into electricity would improve the energy conversion performance.[99–101] It would be beneficial to have materials that can convert a DC temperature gradient into electricity, since heat engines can change a temperature gradient into mechanical oscillations and time-varying temperatures at the multi-physics memory alloy (MPMA) level. Materials that directly correlate temperature changes with charge creation are particularly suitable for this purpose. A significant proportion of reported implementations consider electromechanical energy conversion, which lowers the efficiency of the global thermal-to-electrical energy transfer and calls for a second conversion stage (using a piezoelectric or electromagnetic coupling). The only exceptions to this is pyroelectric coupling.[98,99,102] Direct heat exchange and associated electro-thermal conversion are made possible by integrating MPMAs with pyroelectric energy conversion and using direct heat transfer from the heated MPMA to the pyroelectric device. This heat exchange also makes MPMA cooling easier, thereby improving performance. The heat engine model was built on the Multi-Physic memory alloy (MPMA) described in Fig. 6b, which exhibits a reverse martensitic-austenite phase transition. This allows for a temperature-dependent increase in magnetization, and when combined with a pyroelectric element, it facilitates the direct conversion of thermal energy into electrical energy.[103–105] In particular, direct heat transfer from MPMA is made possible by employing a pyroelectric element, which also requires a small amount of energy for the mechanical medium. The pyroelectric element is mechanically moved back and forth from the hot source. This element retains the heat generated by MPMA and enables alloys to cool more quickly, increasing the frequency.[106–108] The use of the meta-magnetic Heusler alloy in experiments showed improvements in power densities ranging from 3 to 10 in relation to volume and an approximately 27-fold increase in energy density per cycle. Since the pyroelectric element can be positioned on the hot side, the proposed concept can also be used for any heat engine that uses ferromagnetic materials, such as ferromagnetic shape memory alloys. The technique is modified for high-performance heat engines, such as those that use Ni–Mn–Ga compounds. The effects of magnetic field (up to 9 Tesla) on the shape memory and super-elastic responses of [001]-oriented NiMnCoIn single crystals were systematically determined under compression. Thermal cycling under stress and super-elasticity experiments at selected magnetic fields were conducted to reveal the change in transformation temperatures and critical stress with the magnetic field, as described in Fig. 6c. It may combine electro-thermal (pyroelectric coupling) and electromechanical (piezoelectric or electromagnetic effects) conversion effects. By carefully shaping the energy conversion pathways and thermal courses within the system, it is possible to create small-scale energy-harvesting devices that perform better than typical thermoelectric modules. From that angle, investigating the sizes of materials and devices that can benefit from upscaling would be an intriguing aspect.[109–115]

2.4 Metamaterials

Metamaterials are highly pursued for energy harvesting because they are intentionally constructed structures with remarkable capabilities beyond those of basic materials. Energy harvesting is a green technology that recycles mechanical and atmospheric wave energy and converts it into useful electricity. Metamaterials can improve their energy-harvesting capabilities by varying the amplitude and direction of the input waves or by applying more strain to energy-conversion materials and systems. Integrating phononic crystals, mechanical metamaterials, and mechanical metamaterials into energy harvesting systems, such as acoustic and elastic wave localization and mechanical energy trapping phenomena, has resulted in a massive rise in energy research.[116,117] The unit cells of metamaterials, called meta-atoms, are designed during the design process and then grow into supercells. During the fabrication process, new technologies such as additive manufacturing and 3D printing are used in addition to laser cutting and lithography. Metamaterials in the mechanical regime are divided into two categories: mechanical metamaterials (based on static mechanics) and acoustic metamaterials (based on dynamic waves). Acoustic metamaterials are composed of phononic crystals that exploit local resonance phenomena and Bragg scattering. By adding flaws to the bandgap region, the bandgap is used to control wave energy localization. By concentrating the wave energy, the periodic structure can improve the energy density. Mechanical metamaterials, on the other hand, are constructions designed to demonstrate unusual characteristics and behaviours using static mechanics. Since auxetic structures have a substantially greater effective volume modulus, they can display many stable states through buckling with fluid-like features, potentially maximizing the concentration of vibrational and wave energy. The efficiency and performance of self-generated sensing and energy harvesting can be maximized when paired with energy conversion mechanisms, such as electromagnetic conversion through triboelectric and piezoelectric effects, which can transform mechanical energy into electrical energy.[100,101,103] Research hotspots in energy harvesting include small size, high efficiency, frequency self-adaptation, and wide bandwidth. It is necessary to investigate the potential of active metamaterials for adjustable energy harvesting.

To achieve significant thermal gradients, active control could then be combined with the energy-harvesting subsystem to enable the structure to function autonomously.[104,105,117] To concurrently collect energy and store energy and support structural stress, Steven and Daniel developed multifunctional piezoelectric self-charging structures that combined piezoelectric devices with a substrate layer on thin-film lithium batteries.[118–120] An adjustable acoustic waveguide constructed within a 2D phononic plate with a periodic array of piezoelectric transducers switched *via* passive inductive circuits was experimentally demonstrated by Casadei *et al.*[106] With this type of adjustable acoustic metamaterial, the system's dispersion may be controlled to accelerate the generation of bandgaps at specific frequency ranges without changing the crystal's lattice constant. Using spin-torque oscillators, Tatara *et al.* proposed an active metamaterial for electromagnetic radiation at a frequency of GHz.[121] The aim of vibro-acoustic or electromagnetic metamaterials is the extension of metamaterials towards thermal energy harvesting. Theoretically, for ferromagnetic materials composed of cobalt, iron, and gadolinium within their Curie temperature range, thermomagnetic production has an operational Carnot efficiency value of 55%; nevertheless, the values obtained experimentally are significantly very modest. Even the current generation of thermomagnetic demonstrations uses mechanical motion, such as rotation, oscillation, to indirectly convert energy or direct thermal-to-magnetic energy conversion.[67,92,108] The need for special materials exhibiting large changes in magnetization at small temperature differences and several engineering challenges associated with the strong thermomagnetic-mechanical coupling of system properties and various loss mechanisms, including friction, magnetic stray fields, and parasitic heat transfer, pose significant challenges. Experiments on a millimeter-scale TM energy harvesting device demonstrated that micro/nanoscale systems can operate at substantially higher frequencies because of the improved surface-to-volume ratio, which enables the generation of bigger power outputs. Large rapid variations in magnetization around room temperature have been made possible by recent advancements in the creation of Heusler alloys, opening up new possibilities for the conversion of thermal energy to electrical energy. The calculations indicate that even for modest temperature differences of 5 K and magnetic fields of 3 kOe, the efficiency will be in the range of 16% of the Carnot limit. Heusler alloys provide thermomagnetic production under certain conditions. It would be appropriate for TM manufacture to use meta-magnetic Heusler alloys such as Ni–Co–Mn–Z (Z = In, Sn) where a first-order ferromagnetic austenite phase transformation takes place towards a non-ferromagnetic martensite phase.[85–102] The phase transformation temperatures were adjusted by adjusting the chemical composition. A greater temperature differential is a benefit of employing first-order magneto-structural changes. However, there is a hysteresis associated with it that does not exist for the second-order transition. Thus, the choice that produces a better power output greatly depends on the temperature differential and the hysteresis of the material.

2.5 High entropy materials

A class of materials known as high entropy materials (HEMs) has led to the development of technologically appealing properties such as the propensity for single-phase solid solutions with straightforward crystal structures, characteristics that go beyond their constituent elements, and the ability to modify the functional properties.[122–124] A wider variety of materials, such as alloys, borides, nitrides, carbides, phosphides, sulphides, oxides, and oxyfluorides, are included in HEMs. These materials can be used in thermoelectricity applications, electrochemical energy storage, and a variety of catalytic systems. Large entropy will encourage the creation of a single-phase structure with lattice distortion (strain) compared with normal metal complexes. High entropy alloys (HEAs) frequently experience lattice distortions, which are adaptive to gas absorption because they create more favorable reaction sites with potentially advantageous features, particularly for hydrogen storage.[7,123,125,126]

The powerful synergistic effects between the functional units support the exploration of high-entropy noble metal and noble-metal-free electrocatalysts in oxygen evolution and reduction and methanol oxidation, which is advantageous for the catalysis of energy conversion processes. Improved Coulombic efficiency and cycling stability result from the novel entropy-stabilized conversion process demonstrated by HEMs in batteries when used with rock-salt high-entropy oxides (HEOs) as lithium storage anodes.[11,12] The lattice distortions in HEAs, as opposed to metal hydrides, offer significant diffusion pathways and interstitial sites for hydrogen atoms, resulting in an advantageous reversible phase transition upon hydrogenation/dehydrogenation cycling, leading to a balanced storage route.

In contrast to rapidly evolving sorbent materials for hydrogen storage, such as MOFs, the gravimetric capacity of HEAs (usually less than 2.5 wt%) for hydrogen storage has not yet demonstrated clear benefits. The enhanced reaction thermodynamics of HEAs outweigh the drawbacks of MOF-based materials, which need to be cryogenic. The original lattice structure is largely preserved during electrochemical cycling due to the entropy-stabilized reaction mechanism, which acts as a host for the conversion process and improves stability.[123,125] These conversion-type materials still have some intrinsic limitations, such as a low overall energy density due to unfavorable lithiation voltage, low energy efficiency due to large voltage hysteresis, and a detrimental impact on cycling performance and stability due to continuous electrolyte decomposition caused by extrinsic instabilities. Given the large energy consumption of industrial and urban sectors, waste heat recovery for thermal energy production is particularly interesting. The majority of the waste heat energy that is not recovered is found in the low-temperature range or between 10 and 250 °C. Energy conversion is useless when the temperature difference is minimal. The Seebeck effect is the most well-established method for producing thermoelectric energy at low temperatures.[98–101] Nevertheless, downscaling constraints apply to thermoelectric generators, and a significant temperature differential of at least 100 °C is necessary to attain 5% efficiency. Fig. 7a illustrates the chart of potential applications of high-entropy materials.

The primary focus will be on the alloys with no hysteresis, and for that purpose, a Heusler system of alloys having a first-order magneto-structural phase transition (FOMSPT) would be a suitable choice. The high entropy effect promoted the production of single AB2C14 Lave-structured alloys, and the first HEA in this category was FeMnCoTi$_x$V$_y$Zr$_z$. This alloy was used in hydrogen storage studies, and its hydrogen absorption can be improved by substitution of Cr with Co.[7,122] Consequently, the high-entropy effect in the particular complex system favors an efficient and straightforward method of designing the HEA composition because it allows for the optimization and customization of the hydrogen storage properties through the substitution or variation of specific elements without altering the crystal structure.[124,125,127] The lattice distortion in the HEA was supposed to be beneficial for high hydrogen storage capacity (higher than any of its constituent elements can absorb). Several nanoporous AlCoNiFeX-based HEAs with high-entropy (oxy) hydroxide surfaces (X = Nb, Mo, Cr, V, Zr, Mn, Cu) were produced by Qiu and associates.[11] It was shown that the alloy's composition is a key factor in improving the OER performance, with AlCoNiFeMo, AlCoNiFeNb, and AlCoNiFeCr exhibiting the maximum activity. Nanoporous AlNiCuPtPdAu with a ligament structure was created by Qiu *et al.*, and by de-alloying a tailored precursor alloy, the composition could be accurately adjusted.[12] After 100k cycles, this HEA demonstrated ten times the mass activity of Pt/C and an activity retention of about 92.5% for ORR. Fig. 7b plots $(\mathrm{H/atom})_{\max}$ *vs.* ΔH_{cal}. A plot of $(\mathrm{H/atom})_{\max}$ against ΔH_{cal} is linear for A_2B and AB_5 alloy systems, but spreads over a wide range and is highly non-linear for Ti$_x$, V$_y$, and Zr$_z$, AB and AB_2 alloy systems. The factor that dominates the maximum hydrogen storage capacity $(\mathrm{H/M})_{\max}$ is the affinity between the alloy elements and hydrogen. Ti and Zr are involved in hydrogen absorption in CoFeMnTi$_x$VZr and CoFeMnTiVZr$_z$ alloys,

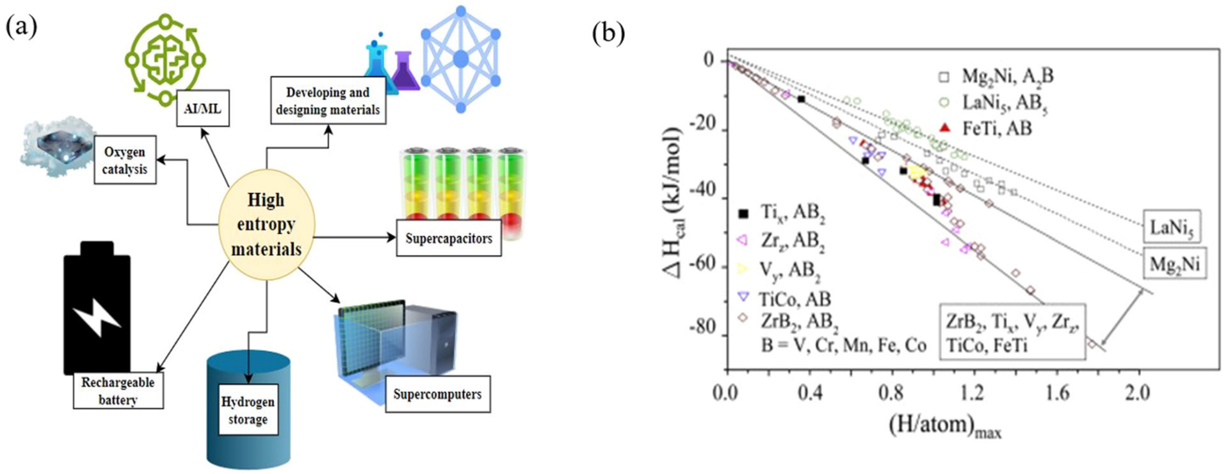

Fig. 7 (a) Chart of potential applications of high entropy materials. (b) The $(\mathrm{H/atom})_{\max}$ *vs.* ΔH_{cal} curves for Mg_2Ni, $LaNi_5$, TiFe (AB), TiCo (AB), ZrB_2 (AB_2), Ti$_x$, V$_y$, and Zr$_z$. It shows that $(\mathrm{H/atom})_{\max}$ is a linear function of ΔH_{cal} for Mg_2Ni, $LaNi_5$, but not for AB, AB_2, Ti$_x$, V$_y$, and Zr$_z$. The alloys AB, AB_2, Ti$_x$, V$_y$, and Zr$_z$ have data scattered over a wide range indicated in this figure. Reproduced with permission.[7] Copyright 2010, Elsevier.

respectively. $(H/M)_{max}$ increases with x and z in the ranges $0.5 \leq x \leq 2$, and $0.4 \leq z \leq 2.3$, respectively. The decrease in $(H/M)_{max}$ values in the Ti2.5 and Zr2.3–3.0 alloys was attributed to the serious segregation of Ti and Zr. Following hydrogen desorption, a large amount of hydrogen is retained in alloy Zrz because of the strong bonding between Zr and H.[128]

2.6 Magneto-electric and caloric materials

Magneto-electric materials are versatile because they can convert magnetic energy to electrical energy and *vice versa*. This capability is useful for creating resourceful magneto-electric generators due to the coupling between magnetic electric properties, which allow for the control of one property by applying the others. This coupling can be exploited in various ways to initiate energy applications.[129–131] Through electromagnetic energy harvesting, materials can be developed to convert ambient electromagnetic radiation, such as radiofrequency or microwave signals, into usable electrical energy for low-power electronic sensors. Certain ferrites are used for developing inductors and transformers and contribute to the effective transfer of energy through inductive energy storage and release. There exist electromagnetic meta-materials, which are engineered to enhance the efficiency of solar cells, create novel antennas and improve electromagnetic shielding performance by controlling and manipulating electromagnetic waves at the subwavelength scale.[112,131–133] Electromagnetic interference (EMI) shielding materials are crucial in energy systems because they mitigate electromagnetic interference and protect electronic devices from external electromagnetic fields. Magnetic refrigeration relies on the magnetocaloric effect, where it can be used as an energy-cooling system as the material heats up and cools down in response to fluctuations in magnetic fields. Superconductors are the most demanded energy-reaping materials because they exhibit zero electrical resistance and expel magnetic fields. Thus, they are used in energy transmission and storage systems, such as high-performance power cables.[129–132]

Magnetic cooling is an alternative technology that relies on the magnetocaloric effect (MCE), which is schematically shown in Fig. 8a. The magnetocaloric materials (MCM) used for MCE application show temperature-dependent magnetic responses. MCMs must possess low synthesis costs, high performance, environment friendly and readily available to develop effective magnetic cooling devices. Considering these factors, MnNiSi-based magnetocaloric alloys were found to exhibit a giant MCE effect and a wide range of T_C tunability near room temperature.[6,134–136] Numerous MCMs targeting certain applications have been created during the past 20 years, and several of these applications have also recently gone into commercialization. Unfortunately, the majority of these materials have many drawbacks, including expensive manufacturing costs, poor mechanical strength, corrosion, low magnetocaloric characteristics, strategic restrictions, and laborious synthesis processes. Mn-based alloys have demonstrated enormous magnetocaloric characteristics among the MCMs studied so far. To induce ferromagnetic interactions, the Mn–Mn interatomic gap can be tuned systematically. Considering the cost of the raw materials, MnNiSi alloy was selected as the foundation material. At 1200 K and 600 K, this alloy shows signs of structural alterations and magnetic transitions. MnNiSi substitutional alloying can lower the T_C and cause a linkage of the structural and magnetic transitions.[65,66,137,138] Fe can substitute an element and lower the temperature by up to 438 K. The T_C must be further lowered to almost room temperature, for example, by double-element substitution with Fe and Ge. Thermomagnetic response of a thermomagnetic alloy (TMA) $(MnNiSi)_{1-x}(Fe_2Ga)_x$ to be exploited by fabricating a prototype like TM oscillator. It is created as a hybrid spacer connecting the heat sink and the load to a permanent magnet. The cooling and heating cycles produce a refrigerating atmosphere of up to 70 K per cycle within a voltage of around 110 V by the coupled oscillations. Figure of merit analysis and simulation models were used to optimize the material qualities and device parameters.[65,66,94,115] The flexible spacer $(MnNiSi)_{0.68}(Fe_2Ge)_{0.32}$ exhibited the highest figure of merit with an oscillation frequency of 32% and a voltage per cycle value of 18% in comparison with a rigid spacer, as illustrated in Fig. 8b. A small-scale thermal energy harvesting prototype based on temperature gradients is proposed as an alternative to traditional thermoelectric modules.

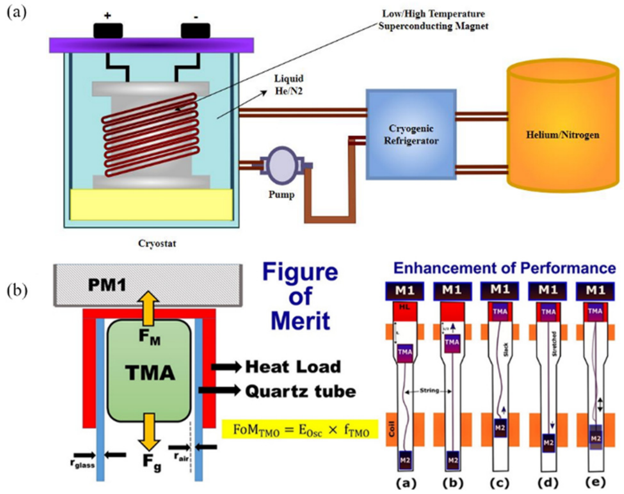

Fig. 8 (a) Schematic of magnetocaloric refrigeration. (b) The prototype of the flexible spacer showing the optimal figure of merit. Reproduced with permission[4] Copyright 2019, Elsevier.

Heat conductivity ($\kappa < 4$ W km^{-1}) in HH materials decreases sharply with the addition of non- and isoelectronic components. Intrinsic phase separation in multi-component HH materials and the resulting higher disorder caused by increased mass and strain fluctuations are responsible for the considerable decline in κ.[31,64,68,74] The addition of nano- or microstructures is another way to alter thermoelectric materials. Experiments on-site replacement of HH compounds significantly improved the TE performance of HH materials. Owing to their high melting points, HH materials have extraordinarily stable intrinsic phase separation at room temperature; this characteristic may be the key to their high TE efficiencies. The Peltier effect is used in thermoelectric cooling, where heat is transferred from one side to the other by an electric current passing across a junction between two distinct conducting materials. The typical intermediate bandgap structure of half-Heusler alloys allows them to efficiently capture and convert various electronic states, thereby improving their electrical conductivity and, consequently, the Seebeck coefficient. This property may help improve thermoelectric performance.[72,73,139] This makes it possible to convert electrical energy into a thermal gradient, which is crucial for cooling systems that require quick, accurate, and rapid temperature control.[10,123,134]

The research happening at present on half-Heusler compounds is aimed at identifying pathways that would help improve their thermoelectric properties.[73,85,138] There are certain approaches to achieve higher *ZT* in half Heusler alloys comparable to that of state-of-the-art materials targeting structural order, heavy hole bands, degeneracy, microstructure and dopant resonant states. Some thermoelectric modules based on half-Heusler compounds exhibit competitive thermoelectric conversion efficiency and power density. Half-Heusler compounds provide advantages in terms of thermal stability and scalability, but before they can be used in real-world devices, significant problems, including material lifespan and robustness, must be resolved. Recent developments have shown that adjusting the composition of already-existing compounds can greatly enhance the thermoelectric capabilities of half-Heusler compounds. TiNiSn and NiTiSn have been explored as compact cooling solutions in scenarios where weight and space constraints are critical contemplations.[65,66,115] The fact that band-structure engineering and microstructure design offer great potential to significantly improve this class of materials is now clear. Notably, new research has highlighted the importance of electron orbitals and valence effects. Owing to the wide range of compositions found in half-Heusler compounds, it is possible to create new compositions that validate and optimize the TE characteristics. The development of several high-throughput techniques that use *ab initio* calculations, machine learning, first-principle thermodynamics, and combinations of these techniques has proved beneficial for material discovery in recent years.[92,139] As the database grows and new algorithms are created, the predictive power of these techniques improves. This result has clear implications for research on half-Heusler materials. Therefore, it is reasonable to anticipate increased progress in *ZT* and, of equal significance, the development of workable thermoelectric generators based on half-Heusler compounds.[31,68,72] The absolute value of the Seebeck coefficient decreases as the total amount of secondary phases increases due to their metallic behaviour, as shown in Fig. 9a. Accordingly, the electrical conductivity increases as the total amount of secondary phases increases, Fig. 9b even if the relationship between these two quantities is less evident than the corresponding trend of the Seebeck coefficient, Fig. 9a. The larger spread of the data in Fig. 9b can be explained by the significant difference in density of the samples (from 80% to almost 100%), which strongly affects the results of measurement of the electrical conductivity. In Fig. 9a and b, the experimental values of the Seebeck coefficient and electrical conductivity as a function of the number of secondary phases are compared with the values calculated by applying the EMT and WJC-EMT (continuous lines), GEMT and WJC-GEMT (dashed lines) models. For values of the secondary phase fraction lower than 40%, the GEMT and WJC-GEMT models predict larger values of σ and lower values of $|\alpha|$, respectively, with respect to the EMT and WJC-EMT models, due to the percolating effect of the metallic secondary phases.[10]

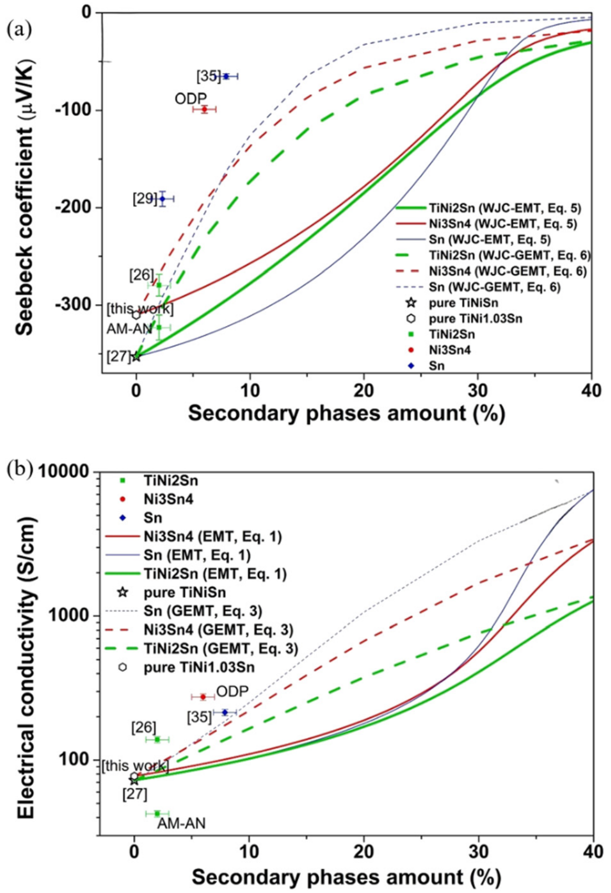

Fig. 9 Seebeck coefficient (a) and electrical conductivity (b) as a function of the secondary phase amount at 328 K. Symbols represent experimental values of the thermoelectric properties taken from the literature and this work. Solid symbols with different shapes and colors refer to samples containing different types of secondary phases. Open symbols refer to pure reference samples (*i.e.* TiNiSn and TiNi$_{1.03}$Sn). Continuous lines with different thickness and colors represent the calculated thermoelectric properties as a function of the amount of each secondary phase, based on the effective medium theory. Reproduced with permission.[10] Copyright 2020, Elsevier.

3 Emerging materials

3.1 Topological quantum materials

Heavy element-containing Heusler compounds are a class of topologically non-trivial systems. At the Γ point, these systems show zero bandgap because of their cubic form. By applying strain, they can be easily steered to the topological insulating state, where their inverse band structure results in a finite bulk band gap. This was initially observed experimentally in CdTe/HgTe/CdTe quantum wells, where the strain in the HgTe spacer

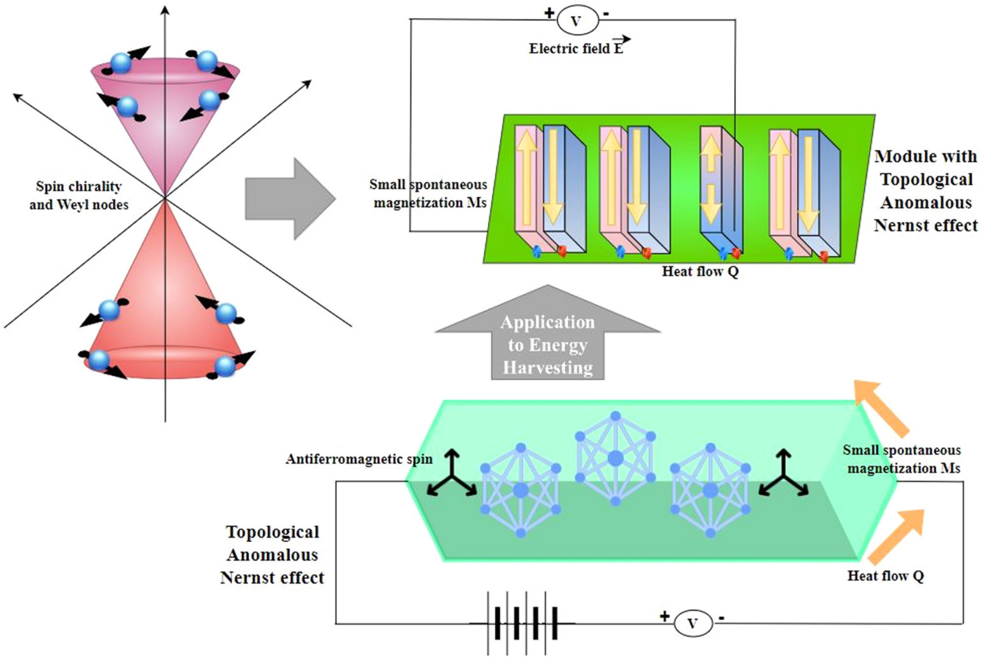

Fig. 10 Topological quantum materials: the diagram shows the connection between Weyl nodes and the Nernst effect. When a Weyl semi-metal is subjected to a magnetic field, Nernst current is generated, and it is perpendicular to field and temperature gradient. The linear dispersion and chirality of the Weyl nodes lead to a non-trivial Berry curvature, which in turn is responsible for the Nernst effect.

generated the TI state. Cubic HgTe crystallizes in the zinc blende structure, linked to a half-Heusler-type structure. The half-Heusler-type cubic HgTe TIs are more flexible and exhibit proximity effects such as superconductivity and magnetism.[140–143] The only way these known TIs can become magnetic or superconducting *via* doping with exogenous elements such as Cu, Fe, or Mn. Fig. 10 shows the topological electronic structure for the development of basic energy harvesting technology.

New magnetic materials, magnetic semiconductors, and half-metallic ferromagnets (HMFs) must be developed to fulfill the potential of spintronics. HMFs meet all of the requirements for spintronics because of their distinct electronic structure, which allows electrons to move in both the same way as semiconductors and in the same direction as metals. Developing a semiconducting material with ferromagnetic properties has required a great deal of work. Although Mn-doped GaAs was considered a promising combination, it is not appropriate for application in electrical devices due to its low Curie temperature of approximately 150 K.[44,141,144] Since the last ten years, topological quantum materials, or TQMs, have been used in information technology, sensing, energy conversion and storage (including electro-oxidation of ethanol), supercapacitors, batteries, water splitting, and other energy-efficient devices. Their quantum states, which offer a steady electron bath with excellent electrical conductivity and carrier mobility, are the cause of their notoriety. TQMs are an excellent platform for comprehending surface reactions because of their long lifetime and easily determinable spin states. The catalytic behaviour of the TQMs begins with the bismuth chalcogenides, which are three-dimensional topological insulators (TIs).[145–147] TQMs with robust topological surface states (TSSs) can resist perturbations such as defects, doping and surface modification. During the photocatalytic hydrogen evolution process, TSS can shield the electrons on the TI (such as Bi_2Se, Bi_2Te and Bi_2Te_2Se) surface from recombination. TaP, NbP, TaAs, and NbAs are examples of Weyl semi-metals, which are transition metal monophosphatides with high mobility between TSS and surface adsorbates. Therefore, they catalyse the hydrogen evolution reaction (HER).[148–150] Additionally, alloy combinations can be used to improve and fine-tune the catalytic capabilities, creating a new route for the use of inexpensive silicon-based options for HER. In NiSi WSMs with hybrid Weyl states and extended surface semi-arcs at the Fermi level, topological charge carriers have recently been shown to participate in the HER process. Oxygen evaluation reactions, or OERs, have recently been discovered through strain, doping, vacancy introduction, defect introduction, and even transition-metal coordination tuning. Nevertheless, these tactics are intimately associated with structural instability because they depend on extrinsic disorders.[151–153] TSM $Co_3Sn_2S_2$ bulk single crystals are a variant of ternary Heusler compounds with robust surface states and high electrical conductivity at room temperature. The e_g–p-orbital overlap strengthens the π–σ and σ^*–π^* bonding (sp and sp^2 hybridization) with the adsorbates, and the active sites transfer electrons to enhance the OER performance. These findings highlight the use of TSSs as active sites in the design of high-efficacy catalysts, such as the state-of-the-art RuO_2 catalysts.[146,153,154]

To explain the genesis of catalytic activity, topological quantum catalysts exploit their topologically protected surface bands as active sites instead of strain, dopant, vacancy, edge or heterostructure-generated sites. Thermoelectrics, supercapacitors, and high-performance battery materials are compatible with the topological characteristics of TQMs. Contrary to the investigation of topological properties like resistivity and anomalous Hall effects, chemical reactions typically occur in harsh environments like acidic, alkaline, or even high vacuum environments, making it difficult to observe topological effects in the field. Thus, spectroscopy is required for the *in situ* monitoring of band topology. One well-studied example is $MoTe_2$, where changes in carrier motilities, hall resistivities, conductivities and surface composition before and after electro/photo-catalytic processes allow one to identify the contribution from the topological phase.[140,142,155,156] Finding a TQM catalyst to use in processes on an industrial scale is quite difficult. Low current densities and potentials are the main emphasis of kinetic and stability analysis for most catalysts and conversion reactions. Increasing the applied potential could destroy the catalysts' surface. Studies have demonstrated that for all redox processes, electrons can be transported concurrently in both charge and spin and that by adjusting the spin polarization, radical pair effects can be used to increase the catalysis efficiency. Regardless of the polarized electrons in magnetic catalysts, permanent magnets created by modulating spin polarization exhibit a 150% increase in the OER current density. Remarkably, the spin pinning effect preserves the spin characteristics, so that the detrimental effects of surface oxidation and rebuilding are mitigated. Although magnetic fields have beneficial impacts, they can inhibit intrinsic catalytic activities. In the instance of TSM Co_2MnGa, for example, the turnover frequency was reduced by 33% as an HER catalyst, while efficiency was increased by 11% for NbAs and 95% for NbP.[73,141,147,149,150,153] Hence, the interplay between magnetic fields and spin-polarization interactions with chemical reactions can be promoted as a current topic of interest in the arena of energy research.

3.2 Materials for batteries and supercapacitors

Lithium-ion batteries (LIBs) have long been the predominant technology in consumer electronics and transportation applications. The prevailing LIB design involves graphite anodes and lithium metal oxide cathodes, typically composed of layered materials.[157–159] There is a call for the exploration and development of novel electrode materials to address the growing demand for increased energy and power density. Silicon emerges as a promising candidate on the anode front, boosting a 10-fold higher specific capacity (4200 mA h g^{-1} for silicon, compared to 372 mA h g^{-1} for graphite).[160] However, a significant challenge lies in its substantial volume change—four times—between charged and discharged states, posing a risk of mechanical failure. Over the past decade, various nanoscale design solutions have been proposed to counteract mechanical fracture and solid–electrolyte interphase instability associated with silicon anodes. Another intriguing option is lithium metal anodes, known for their high capacity (3860 mA h g^{-1}).[161] Despite their potential, challenges such as limited battery lifespan, dendrite formation, low cycling, reduced Coulombic efficiency, and safety concerns have hindered their commercialization. Pursuing advancements in electrode materials remains critical to overcome these challenges and pave the way for the next generation of high-performance batteries. In grid-scale applications, crucial considerations include cost, scalability, and long cycle life. Redox flow batteries exhibit promise for grid storage, which separates positive and negative electrolytes. Semi-flow batteries, exemplified by Zn–halogen and Li–polysulfide systems (employing one solid and one liquid electrode), eliminate the necessity for ion-selective membranes, potentially leading to cost reduction.[162,163] Moreover, ongoing research is exploring the replacement of lithium (Li) with more sustainable chemistries based on sodium (Na), potassium (K), magnesium (Mg), and aluminum (Al). However, for these alternative technologies to become competitive, a comprehensive re-evaluation and tailored development of all battery components—namely, the anode, cathode, solvent, salt, and additives—is imperative.[164] In addition to self-healing polymers, shape-memory alloys like NiTi can be added to Li-ion battery anodes to repair anode material fissures caused by repeated Li insertion and extraction.[165,166] After thermal cycling, the thermal expansion coefficient is reduced by the addition of a TiNiHf shape memory alloy mesh with a phase transformation temperature in the targeted range of 250 °C in a glass matrix. These findings raise the prospect of using a thermal-expansion gradient design for active stress relief and crack healing.[157,167] This is predicated on the shape memory-alloy matrix's superelastic recovery and stress-induced martensitic transformation, which reduce internal stress and cause the anode's fissures to close. Therefore, high-rate capabilities and steady cyclability can be achieved. The absence of long-lasting sealing caused by thermal expansion mismatches prevents solid oxide fuel cells from being used widely. Due to these alloys' superior mechanical qualities, biocompatibility, corrosion resistance, and processability, extensive research has been conducted on them. These alloys can be utilized as active components in electrocapacitive wire electrodes, which can be used as shape memory supercapacitors.[164,168] When subjected to plastic deformations, these alloys can automatically return to their original, undistorted state a few seconds above the temperature at which heat activation occurs. Additionally, by incorporating these shape memory supercapacitors with conventional textiles, a smart sleeve was created. This sleeve exhibits a variety of unique functions, including the ability to automatically cool down when it becomes too hot and return to its original shape.[165,167] The Kapton tape is used to peel off the CNT/Ni/CNT forest (top in Fig. 11a). Packaged supercapacitors are tested under different bending angles from 30 to 90 degrees, as shown in Fig. 11b. Results in Fig. 11c shows the coherent cyclic voltammetry results under different bending angles with little changes. Using a scanning rate of 200 mV s^{-1}, the flexible supercapacitor shows a projection capacitance of ~ 10 mF cm^{-2}. The low ion mobility in the solid-state electrolyte and high electrolyte–electrode resistance results in low specific capacitance. The prototype package also causes low specific volume capacitance, which can be improved by thinning the packaging substrate. The cyclic CV tests in

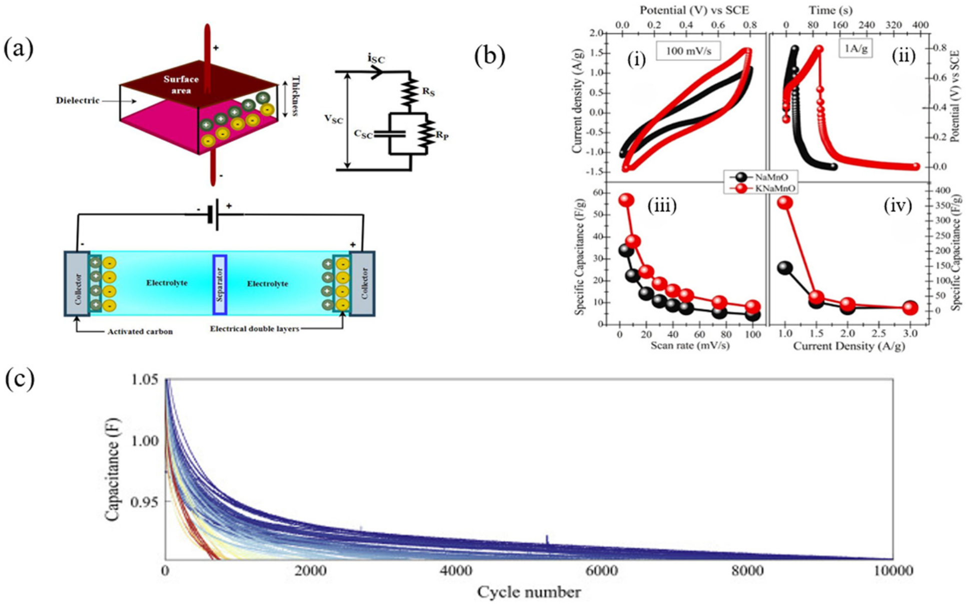

Fig. 11 (a) Working principle of a supercapacitor. (b) Electrochemical performance of NaMnO and KNaMnO samples, (i) CV curves, (ii) GCD curves, (iii) specific capacitance *versus* scan rate, and (iv) specific capacitance *versus* current density. Reproduced with permission, Copyright 2024, Elsevier. (c) Discharge capacity for the first 10 000 cycles of 88 tested supercapacitors (SCs), where all SCs exhibit rapid capacitance degradation in the beginning and slow capacitance degradation in the end. Reproduced with permission,[9] Copyright 2020, Elsevier.

Fig. 11d for over 10 000 cycles show good stability with over 90% retention. The inset of Fig. 11d also shows the impedance measurement of the CNT/Ni/CNT electrode with low AC resistance.[8]

Supercapacitors are energy storage devices that fill the void left by conventional capacitors and batteries,[169–173] and nanostructures are essential to their advancement. The working principle of a simple supercapacitor is illustrated in Fig. 12a. Accomplished with distinct characteristics, nanostructured materials allow for faster charge–discharge cycles and Fig. 12 improved energy storage. Supercapacitors operate better overall thanks in large part to the huge surface area and customized features of nanostructures.[174–176] The high-performance electrode is necessary for creating high-power, voltage-efficient semiconductors and the materials that show superior conductivity, are electrochemically stable and are light-weight are the CNTs and graphene due to larger specific surface area (SSA) (430–1600 $m^2\ g^{-1}$) and capacitance. A single graphene sheet has a surface area of 2630 $m^2\ g^{-1}$. Porous graphene, reduced graphene oxide, graphene/CNT, graphene/rGO-conducting polymers, graphene fibers, graphene films, graphene aerogels, and graphene foams are common components of graphene-based supercapacitors.[8,49,177] Supercapacitors have a lower specific energy than batteries despite their many benefits. High specific capacitance, electrical conductivity, and superior electrochemical stability have been demonstrated in metal oxides, which makes them excellent choices for high-performance supercapacitor (SC) electrodes.[166,175] This behavior of SCs is shown in Fig. 12c. Metal oxides can hold more charge for their mass or volume regarding specific capacitance, which is often higher in metal oxides. Some examples of metal oxides with high specific capacitance and good reversibility are ruthenium oxide (RuO_2), cobalt oxide (Co_3O_4), nickel oxide (NiO), and manganese oxide (MnO_2). Fig. 12b shows the electrochemical behavior (capacitance) of NaMnO and KNaMnO. It is interesting to note that oxide materials are less expensive, less hazardous, have a higher energy density than carbon materials, and have more stability than conducting polymers. Polymers were considered insulators until their discovery in terms of conjugate (conducting) polymers having optical and electrical properties similar to organic semiconductors. One of the first conducting polymers, polyaniline (PANI), is synthesized chemically or electrochemically.[159,174,178] In certain applications, such as electronics, optoelectronics, and catalysis, epitaxial hybrid nanostructures have significantly improved performance compared with individual materials or non-epitaxial hybrid nanostructures because of their well-defined chemical compositions and structural features. Core–shell nanostructures, such as 0D nanoparticles and nano polyhedrons; 1D nanorods and nanowires; and 2D nanoplates, nanoplatelets, and nanosheets, are examples of epitaxial hybrid structures. A synergistic effect between the components occurs regardless of the growth mode; in other words, epitaxial and non-epitaxial growth exhibit the synergistic effect.[162,174,178] The controlled synthesis of epitaxial hybrid nanostructures with desired components, topologies, architectures, and crystal phases remains a remarkable problem despite the creation of several epitaxial hybrid nanostructures. Engineering seeds for epitaxial growth could be one approach to very controlled growth. The fundamental mechanisms for producing these hybrid nanostructures still need to be fully understood, even though several synthetic techniques for their epitaxial development have been devised.[78,179]

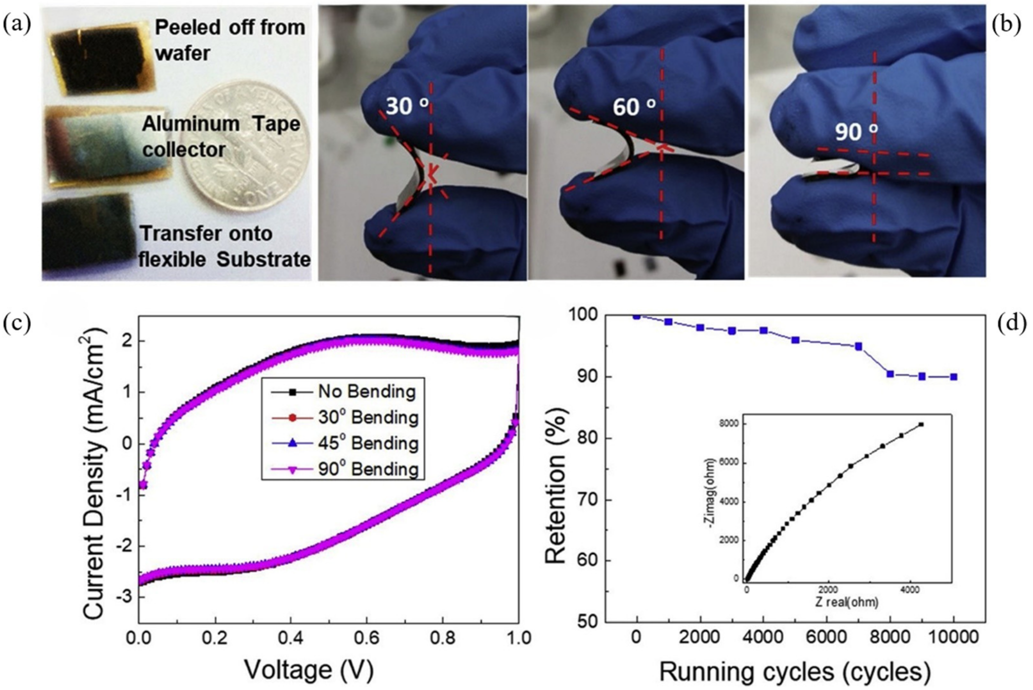

Fig. 12 (a) and (b) Packaging of the flexible supercapacitor based on two CNT/Ni/CNT electrodes and the H_3PO_4/PVA solid-state electrolyte. The Kapton tape is used to peel off the CNT/Ni/CNT film from the SOI wafer, and a stainless steel is taped at the back side as both charge collector and mechanical supporter. (c) Cyclic voltammetry of a flexible supercapacitor under different angles, with a scanning rate of 200 mV s^{-1}. (d) 10 000 cycles CV test of the same supercapacitor in (c) using a scanning rate of 2 V s^{-1}. Inset: Impedance measurement of the CNT/Ni/CNT electrode. Reproduced with permission.[8] Copyright 2020, Elsevier.

Hyped as the perfect energy carrier, hydrogen has the advantages of being renewable, eco-friendly, and a suitable fuel for cars. Despite these benefits, the difficulty of effective storage has limited its practical implementation. Carbon nanotubes (CNTs) have shown great promise as hydrogen storage materials.[180,181] Their capacity to hold a sizable amount of hydrogen at normal temperature was demonstrated by early studies. Nevertheless, problems remained, with contentious outcomes and limitations in replicating research because of complex experimental setups.

Solid-state batteries (SSBs) have attracted increasing attention in recent years due to their potential to overcome the limitations of conventional liquid electrolyte-based batteries, particularly in terms of safety, energy density, and operational stability. A key area of development lies in the identification and optimization of solid electrolytes that combine high ionic conductivity with wide electrochemical stability windows. Among the most studied materials are sulfide-based electrolytes, such as $Li_{10}GeP_2S_{12}$ (LGPS) and argyrodite-type compounds like Li_6PS_5Cl, which offer ionic conductivities comparable to those of liquid electrolytes.[182] However, challenges such as air/moisture sensitivity and interfacial stability with electrodes remain. Recent efforts have also explored halide-based solid electrolytes, particularly Li_3YCl_6 and Li_3InCl_6, which demonstrate high electrochemical stability and better moisture resistance.[183] These halides show promise in enabling full cells with nickel-rich layered oxide cathodes, offering both performance and practicality for commercial development.[184] In parallel with this, oxide-based solid electrolytes such as garnet-type $Li_7La_3Zr_2O_{12}$ (LLZO) and perovskite-type $Li_{3x}La_{2/3}–xTiO_3$ (LLTO) have gained traction due to their superior thermal and chemical stability.[185] Among these materials, LLZO is particularly notable for its relatively high ionic conductivity and compatibility with lithium metal anodes. However, the rigid nature of oxides often leads to poor interfacial contact with electrodes, necessitating surface modifications, buffer layers, or the use of polymeric interlayers to enhance adhesion and reduce interfacial resistance.[186] Recent studies have introduced doped LLZO, such as Ta-doped or Al-doped variants, which not only stabilize the cubic phase at room temperature but also improve the sintering process to yield dense and conductive ceramics.[187,188] Such innovations are critical for the practical implementation of oxide-based SSBs.

In addition to solid electrolytes, cathode and anode materials tailored for solid-state configurations are also under rigorous investigation. For instance, sulphur-based cathodes are being incorporated into solid-state architectures to form all-solid-state lithium–sulphur batteries (ASSLSBs).[189,190] These systems benefit from the high theoretical capacity of sulphur while avoiding the typical polysulfide shuttle effect in liquid electrolyte systems. A recent approach involves embedding sulfur into conductive carbon frameworks and integrating them with sulfide electrolytes, such as Li_6PS_5Cl, to enhance electronic conductivity and ionic diffusion pathways.[191] On the anode side, lithium metal remains the ideal candidate due to its ultra-high specific capacity. However, dendrite formation remains a concern. Advanced interfacial engineering strategies, such as the deposition of thin buffer layers (*e.g.*, $LiNbO_3$ or LiF), as well as the use of lithiophilic interlayers, are being actively developed to stabilize lithium plating and stripping in solid-state configurations.[189,192]

Beyond solid-state batteries, researchers are also developing novel battery chemistries, such as lithium–air and lithium–sulfur systems, to meet the growing demand for ultra-high energy density. In the lithium–air battery domain, recent breakthroughs have come from the use of solid-state and gel–polymer electrolytes to mitigate the challenges associated with oxygen crossover and moisture sensitivity.[193,194] For example, composite electrolytes combining polyethylene oxide (PEO) with ceramic fillers like LLZO have been employed to provide flexibility and ionic conductivity, thereby stabilizing the electrochemical window and extending the cycle life. In addition, research into highly porous carbon-based cathodes with embedded catalysts such as MnO_2 or Co_3O_4 has shown to promote reversible oxygen reduction and evolution reactions, a critical factor in improving the efficiency and cyclability of lithium–air systems.[161,195] Finally, sodium-ion and potassium-ion batteries are emerging as cost-effective alternatives to lithium-based systems, particularly for grid-level energy storage.[196] The use of abundant and geographically distributed elements makes these batteries economically and strategically favorable. Recent work in sodium-ion batteries has focused on layered oxide cathodes such as Na_xMnO_2 and polyanionic materials like $Na_3V_2(PO_4)_3$, which offer decent capacity and stability. On the anode side, hard carbon remains the most viable option due to its ability to accommodate large sodium ions.[184,197–199] Similarly, potassium-ion batteries benefit from graphite anodes—an advantage over sodium, which typically fails to intercalate into graphite. Researchers are exploring Prussian blue analogues as cathode materials due to their open framework and high-rate capability.[200,201] In both battery types, efforts are also being directed toward developing compatible electrolytes, including ionic liquids and gel-based formulations, to enable high-voltage and long-term operation. These advancements reflect a broader trend in battery research: designing tailored materials to support the next generation of safe, high-performance, and sustainable energy storage systems.

3.3 MXenes

MXenes are a relatively new class of two-dimensional materials, typically composed of transition metal carbides, nitrides, or carbonitrides.[202–204] They are derived from layered MAX phases (where M is an early transition metal, A is an element from groups 13–16, and X is carbon and/or nitrogen) through selective etching of the "A" element. The result is a layered structure with exceptional electrical conductivity, mechanical flexibility, and rich surface chemistry. These characteristics make MXenes highly promising for various energy-related applications.[202,205] In particular, their large surface area, tunable electronic structure, and hydrophilic surfaces enable efficient charge transport and ion intercalation, which are crucial in devices such as supercapacitors, batteries, and thermoelectric generators. Additionally, MXenes exhibit piezoelectric and triboelectric properties under certain conditions, opening avenues for mechanical-to-electrical energy conversion. Furthermore, their high photothermal and plasmonic activity makes them useful for solar energy harvesting and photodetectors. The ease with which their surface can be functionalized also allows for the tailoring of their properties to meet specific energy conversion and storage needs. Collectively, these traits position MXenes as a multifunctional platform in the pursuit of efficient next-generation energy harvesting technologies.[202,206–208] These materials serve as excellent electrode materials in supercapacitors owing to their high electrical conductivity and large specific surface area. These properties support efficient charge storage through electrical double-layer capacitance and pseudocapacitance mechanisms. The interlayer spacing in MXenes also facilitates rapid ion diffusion, which is critical for high-power performance. Additionally, the flexibility of surface terminations (like –OH, –F, –O) can be used to tailor the electrochemical behavior.[206] When engineered properly, MXenes can offer high energy density and long cycling stability, making them attractive alternatives to traditional carbon-based or metal oxide electrodes.[204,209] Although MXenes may not be inherently piezoelectric in their pristine form, their composite formulations with piezoelectric polymers or materials like PVDF (polyvinylidene fluoride) have shown great promise. In such hybrid systems, MXenes enhance the charge collection and mechanical strength, boosting the overall power output of piezoelectric nanogenerators (PENGs).[209–211] The incorporation of MXene flakes improves the dielectric constant and facilitates better stress transfer, which increases the piezoelectric response. This makes MXene-based composites effective for harvesting biomechanical energy from motions like bending, stretching, or vibration, with potential applications in self-powered wearable electronics and health monitoring devices. Their layered structure and tunable bandgap allow for the control of carrier concentration and thermal conductivity—two key parameters in thermoelectric performance.[203,204,212] By doping or creating heterostructures, MXenes can achieve a balance between high electrical conductivity and low thermal conductivity, improving the thermoelectric figure of merit (ZT). Additionally, their ability to form flexible films provides another advantage for flexible or wearable thermoelectric generators, particularly in low-grade waste heat recovery.

Fig. 13a shows a schematic illustration of the assembled asymmetric supercapacitor device using Ni_2Co-LDHs@AL-Ti_3C_2 MXene as the battery-type positive electrode and graphene hydrogels as the negative electrode. Fig. 13b shows CV curves of the assembled HSCs device recorded at various scan rates with a potential window of 0–1.6 V. It is clear to observe two broad anodic and cathodic peaks in the CV profiles at all scan rates, which is the combination result of double-layer capacitive and faradaic behavior. As shown in Fig. 13c, the GCD curves show good symmetry at various current densities with a potential window of 0–1.55 V, indicating high Coulomb efficiency and electrochemical reversibility. The sloped voltage profiles with obscure voltage plateaus are the typical features

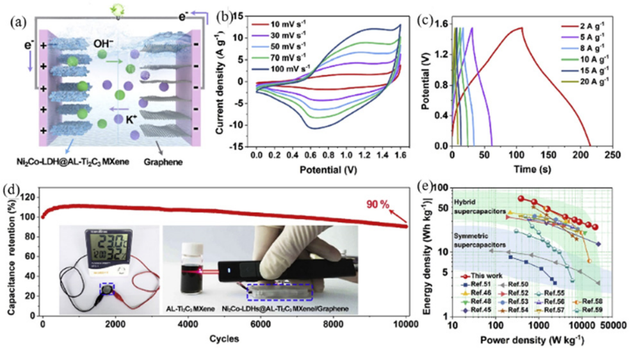

Fig. 13 (a) Schematic illustration of the fabricated HSCs device using Ni$_2$Co-LDHs@AL-Ti$_3$C$_2$ MXene as the positive electrode and graphene hydrogels as the negative electrode. (b) CV curves of the HSCs at various scan rates. (c) GCD curves of the HSCs at different current densities. (d) Cycling stability of the HSC device at 5 A g^{-1}. Insets show photographs of the electronic display powered by HSCs (left) and atomic-layered Ti$_3$C$_2$ MXene suspension irradiated by a laser pointer driven by two tandem devices. (e) Ragone plots of the as-assembled HSCs device and some reported results. Reproduced with permission.[215] Copyright 2020, Elsevier.

of hybrid capacitors, which agrees well with the CV results. The HSC device exhibits a very high specific capacitance of 140 F g^{-1} at 2 A g^{-1}. As shown in Fig. 13d, the durability of the HSCs was further evaluated at 5 A g^{-1} over 10 000 cycles. Remarkably, the HSC device still retains a good capacitance retention of 90% after 10 000 cycles, showing excellent cycle stability. According to the GCD curves, the corresponding energy and power densities are presented as a Ragone plot in Fig. 13e. The as-assembled HSC device delivered a high energy density of 68 W h kg^{-1} at a power density of 388 W kg^{-1}. MXenes have emerged as high-performance electrode materials for supercapacitors, primarily due to their outstanding conductivity and layered structure. One of the most studied MXenes, Ti$_3$C$_2$T$_x$, has demonstrated excellent electrochemical behavior in aqueous and organic electrolytes. For example, Ti$_3$C$_2$T$_x$-based supercapacitors have achieved specific capacitances exceeding 300 F g^{-1} in acidic electrolytes like H$_2$SO$_4$, attributed to the combination of electric double-layer capacitance and surface redox reactions (pseudo capacitance). In particular, the presence of surface terminations such as –OH and –O enhances the ion adsorption and contributes to the overall capacitance. For instance, combining Ti$_3$C$_2$T$_x$ with conductive polymers such as polyaniline (PANI) or polypyrrole (PPy) has resulted in flexible, high-capacity electrodes. These hybrids exhibit synergistic effects: MXenes provide excellent electrical pathways and mechanical support, whereas the polymers contribute additional pseudo capacitance. Some composites have specific capacitances over 500 F g^{-1} and remarkable cyclic stability over 10 000 cycles.[205,213] Another notable approach involves creating 3D porous MXene architectures, which enhance the ion transport and accessibility of active sites. Freeze-drying or templating techniques have been used to prevent restacking of the layers—a common issue with 2D materials. These porous MXene electrodes exhibit not only high capacitance but also fast charge/discharge capability, making them ideal for applications requiring energy and power density.[206,207,211,214] Furthermore, solid-state MXene supercapacitors are being actively developed for flexible and wearable electronics.

Fig. 14a shows typical cyclic voltammetry (CV) curves of the Ni$_2$Co-LDHs@ALTi$_3$C$_2$ MXene and other electrodes at various scan rates. All curves show a pair of strong cathodic and anodic peaks, which is a typical faradaic reaction behavior (battery-type) of a reversible reaction. The CV curves of the Ni$_2$Co-LDHs@ALTi$_3$C$_2$ MXene and its counterparts are shown in Fig. 14b. The Ni$_2$Co-LDHs@ALTi$_3$C$_2$ MXene shows the longest discharging time of 150 s among all samples, indicating higher energy storage, consistent with the CV in Fig. 14c. The Ni$_2$Co-LDHs@ALTi$_3$C$_2$ MXene electrode exhibits the highest peak current density and largest CV integral area among all electrodes, revealing faster faradaic processes and higher specific capacity. The GCD curves of the Ni$_2$Co-LDHs@ALTi$_3$C$_2$ MXene and its counterparts at current densities from 1 A g^{-1} to 300 A g^{-1} were shown in Fig. 14d. All GCD curves exhibit a typical faradaic behavior with a well-defined potential plateau. Based on the GCD curves of all samples, the relationship of specific capacity, current density and IR drop is shown in Fig. 14e. The Ni$_2$Co-LDHs@AL-Ti$_3$C$_2$ MXene exhibits the highest specific capacity and minimum IR drop at all current densities, while the Ni$_2$Co-LDHs shows the lowest specific capacity and maximum IR drop. Fig. 14f gives a visual bar chart with a comparison of the RESR and R_{ct} values of all samples fitted

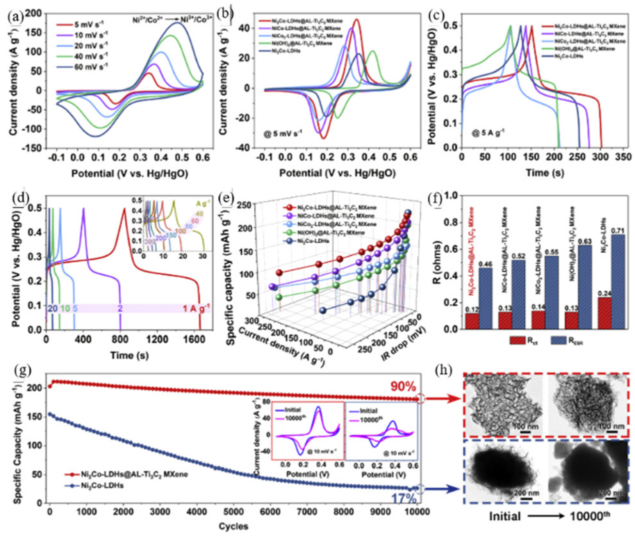

Fig. 14 (a) CV curves of the Ni$_2$Co-LDHs@AL-Ti$_3$C$_2$ MXene electrode at different scan rates. (b) CV curves of the Ni$_2$Co-LDHs@ALTi$_3$C$_2$ MXene at a scan rate of 5 mV s^{-1}. (c) GCD curves of the Ni$_2$Co-LDHs@ALTi$_3$C$_2$ MXene and its counterparts at a current density of 5 A g^{-1}. (d) GCD curves of the Ni$_2$Co-LDHs@ALTi$_3$C$_2$ MXene electrode at different current densities. (e) Relationship of specific capacitance, current density and IR drop of the Ni$_2$Co-LDHs@ALTi$_3$C$_2$ MXene and its counterparts. (f) Comparison of RESR and R_{ct} values of all samples. (g) Cycling performance of the Ni$_2$Co-LDHs@ALTi$_3$C$_2$ MXene and Ni$_2$Co-LDHs electrodes at 10 A g^{-1}, the inset is the CV curves of the Ni$_2$Co-LDHs@ALTi$_3$C$_2$ MXene and Ni$_2$Co-LDHs electrodes before and after 10 000 cycles. (h) Comparison of TEM images of the Ni$_2$Co-LDHs@ALTi$_3$C$_2$ MXene (top) and Ni$_2$Co-LDHs (bottom) before and after 10 000 cycles. Reproduced with permission.[215] Copyright 2020, Elsevier.

by equivalent circuits. As shown in Fig. 14g, the cycling stability of the Ni_2Co-LDHs@ALTi_3C_2 MXene and pure Ni_2Co-LDHs electrodes is checked at a constant current density of 10 A g^{-1} for 10 000 cycles. Remarkably, the capacity retention of the composite electrode can reach ∼90% after 10 000 cycles, much higher than that of the pure Ni_2Co-LDHs electrode (∼17%). As shown in Fig. 14h, the TEM images show that the composite remains in its 3D spatial structure (at top), while the pure Ni_2Co-LDHs aggregated into bigger solid particles (at the bottom). It indicates the cycling stability of electrochemical performance could be attributed to the structural stability of the composite. It also confirms the important role of flexible/stiff interfaces of the Ni_2Co-LDHs@AL-Ti_3C_2 MXene composite, which can prevent the flexible LDHs sheets from aggregation. MXene films integrated with gel electrolytes such as PVA/H_2SO_4 have shown excellent bendability and mechanical resilience without sacrificing electrochemical performance. To further improve thermoelectric efficiency, MXenes are often incorporated into composite materials. One study demonstrated that combining $Ti_3C_2T_x$ with bismuth telluride (Bi_2Te_3) or conducting polymers like PEDOT:PSS can synergistically enhance the thermoelectric figure of merit (*ZT*).[216] In these hybrids, MXene flakes act as conductive bridges and phonon scatterers, facilitating charge transport while impeding heat flow. Thus, composites have achieved significantly higher *ZT* values than the individual components alone. Moreover, solution-processed MXene thin films have opened new possibilities for flexible and wearable thermoelectric devices. These films can be deposited on bendable substrates and still maintain good electrical performance. For example, a flexible thermoelectric generator based on $Ti_3C_2T_x$/PEDOT:PSS layers has been fabricated to harvest body heat, showing stable output under mechanical deformation. Such devices are promising for powering small-scale electronics in self-powered wearables and internet-of-things (IoT) applications.[217–219] Recent advances also explore doping strategies using elements like Se or Te to alter carrier concentration and phonon scattering in MXene structures. These modifications offer precise control over thermoelectric parameters, making MXenes a tunable platform for future energy harvesting devices.[205,220,221] Although challenges remain in optimizing the *ZT* values for room-temperature applications, the combination of flexibility, processability, and multifunctionality makes MXenes a compelling choice for next-generation thermoelectric systems.

In a 2024 study, researchers developed a flexible PENG by integrating poly(vinylidene fluoride) (PVDF) with Ti_3C_2 MXene nanosheets. The addition of 1 wt% MXene significantly increased the β-phase content of PVDF, which is crucial for piezoelectric activity. This composite generated an electrical output of 5 V under finger tapping and achieved a peak-to-peak voltage of 21 V with a short-circuit current of 0.9 μA at a water flow rate of 3 m s^{-1}, demonstrating its potential for underwater energy harvesting applications.[209] Another notable development in 2023 was the creation of a flexible PENG using cellulose nanofibril (CNF) and Ti_3C_2 MXene composite aerogels. The incorporation of MXene improved the mechanical strength and electrical conductivity of the aerogels. The resulting PENG exhibited enhanced performance in harvesting low-frequency mechanical energy, demonstrating the versatility of MXene-based composites in energy harvesting devices.[218,222] Additionally, in 2022, a study reported the fabrication of a PENG using lithium-doped zinc oxide (Li:ZnO) nanowires grown on Ti_3C_2 MXene sheets. This hybrid structure enhances the overall permittivity and facilitates effective polarization during the poling process. The PENG demonstrated a twofold increase in output power density (∼9 μW cm^{-2}) compared to devices without the MXene platform, highlighting the efficacy of MXene in boosting piezoelectric performance.[210] In a 2023 study, researchers investigated black phosphorus (BP) combined with V_3C_2 MXene to form layered heterostructures as sustainable cathode materials for LIBs.[222] The BP/V_3C_2 heterostructure exhibited a notable lithium storage capacity of 630.320 mA h g^{-1}, surpassing many previously reported two-dimensional cathode materials. This enhancement can be attributed to the efficient intercalation of lithium ions within the layered structure, as supported by first-principles calculations. Another study in 2023 focused on the development of an MXene/graphene oxide (GO) heterojunction as a high-performance anode material for LIBs.[222] By employing vacuum ball milling, $Ti_3C_2T_x$ MXene was combined with GO, resulting in a composite that maintained structural integrity and exhibited improved lithium storage performance. After 2000 cycles at a current density of 2.5 A g^{-1}, the composite retained a reversible capacity of 116.5 mA h g^{-1}, demonstrating a capacity retention rate of 116.6%. Further advancements include the synthesis of nitrogen-doped graphene-like carbon (NGC) intercalated $Ti_3C_2T_x$ MXene heterostructures.[223] This design aimed to enhance sodium-ion and lithium-ion storage capabilities. The NGC-$Ti_3C_2T_x$ MXene electrode achieved a reversible capacity of 400 mA h g^{-1} after five cycles at a specific current of 20 mA g^{-1}, demonstrating its potential in high-capacity energy storage applications. Additionally, the integration of silicon nanoparticles with $Ti_3C_2T_x$ MXene was explored to address the challenges associated with silicon anodes in LIBs, such as significant volume expansion and poor electrical conductivity. By electrostatically assembling amino-functionalized silicon nanoparticles with MXene nanosheets, researchers have developed a porous composite structure.[210,211,222,223] This design accommodated silicon expansion and provided efficient pathways for electron transport, resulting in a discharge capacity of 1203.3 mA h g^{-1} after 100 cycles at 200 mA g^{-1}.

3.4 Hybrid materials

Certain materials are now widely used for gas separation and storage. These materials are engineered to selectively capture, store, and release specific gases, contributing to advancements in fields such as gas separation, purification, and storage. Some are metal–organic frameworks (MOFs), zeolites, porous organic polymers (POPs), polymer membranes, activated carbon, and hybrid materials. MOFs are highly crystalline materials consisting of clusters or metal ions coordinated with organic ligands and have a tunable porous size with a high surface area. These classes of materials are illustrated in Fig. 15. They can capture and adsorb carbon dioxide, methane and hydrogen due to their

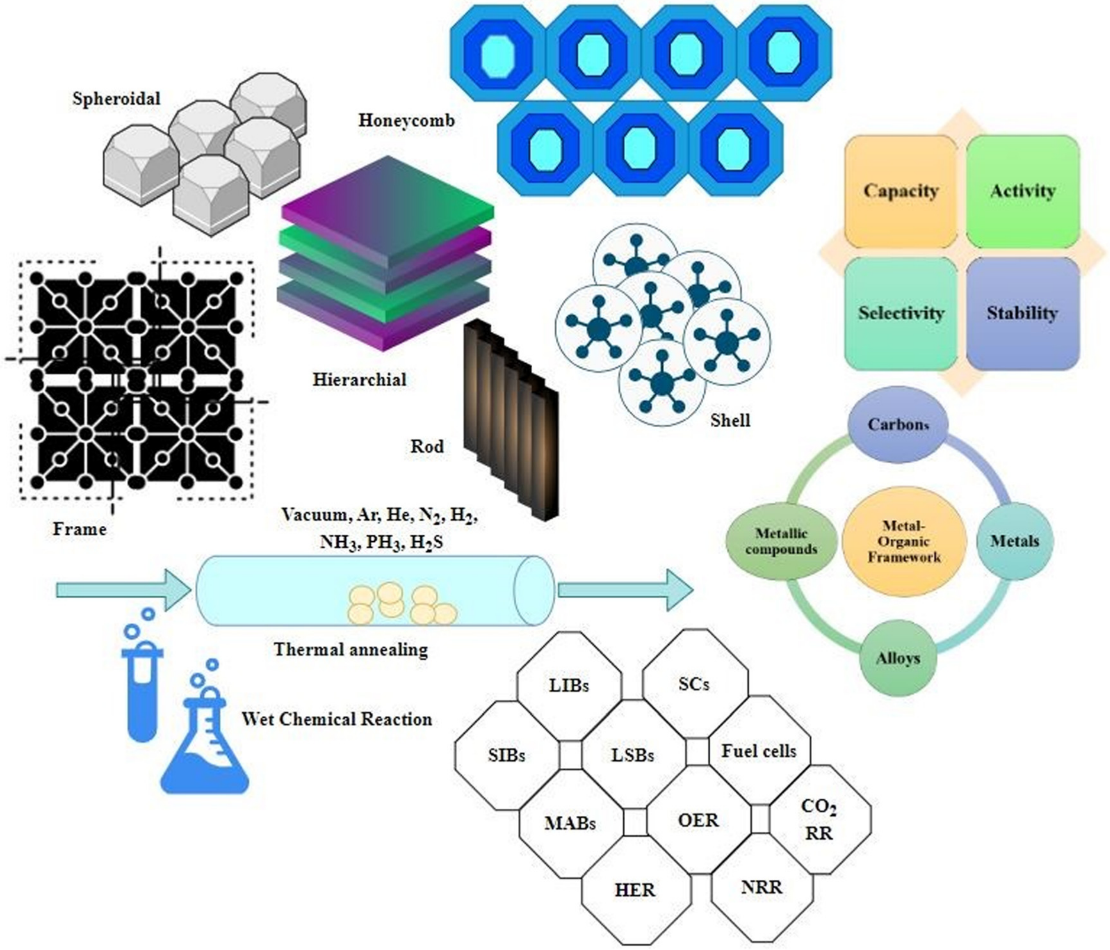

Fig. 15 Diagrammatic representation of metal–organic framework materials.

adjustable structure that would tailor the properties to target those specific gaseous molecules.[49,224,225] For instance, zirconium-based MOFs such as UiO-66 and its derivatives continue to attract attention due to their remarkable thermal and chemical stability. Functionalized versions like UiO-66-NH_2 and UiO-66-SO_3H have shown enhanced performance in CO_2 capture and water adsorption, respectively, by leveraging the introduced polar functional groups to increase interaction with guest molecules.[226] Additionally, iron-based MOFs such as MIL-100(Fe) and MIL-53(Fe) have demonstrated promising capabilities in environmental applications due to their redox-active nature and biocompatibility.[227] The development of conductive MOFs, such as those based on tetrathiafulvalene (TTF) or incorporating π-conjugated linkers, has further expanded the utility of MOFs in electrochemical applications like supercapacitors and batteries, offering porosity and electrical conductivity.[228] Another recent trend involves hybridizing MOFs with other functional materials to improve their practical performance and processability. For instance, MOF-derived carbon materials have gained prominence as high-surface-area electrodes for lithium-ion and sodium-ion batteries. These materials are synthesized by pyrolyzing MOFs such as ZIF-8 or MOF-5 under controlled atmospheres, resulting in nitrogen-doped porous carbon structures that offer excellent electrochemical properties.[229] Similarly, incorporating MOFs with graphene oxide or carbon nanotubes has led to composite materials with enhanced mechanical strength, electrical conductivity, and sorption capacity. In catalysis, MOFs like HKUST-1 and PCN-series materials have been utilized for photochemical and electrocatalytic CO_2 reduction, leveraging their well-defined active sites and large surface areas.[230] Furthermore, advances in post-synthetic modification techniques have enabled the fine-tuning of pore environments and chemical functionalities, allowing MOFs to be tailored for specific target applications, such as selective gas separation or drug delivery. POPs are intrinsically possessed with a pore network, making it very suitable for gas adsorption and separation. In contrast, zeolites are known for micro-porosity and are found to be highly applicable in petrochemical refining and natural gas purification. Activated carbon is widely used for gas adsorption and storage, including removing pollutants from air and water. It is employed in gas masks, air purifiers, and environmental remediation. Polymeric membranes are selective barriers that permeate the specific gases while blocking others and found application in purification of natural gas and the removal of noxious carbon dioxide from industrial emissions.[166,224] Hybrid materials combine different classes of materials, such as organic and inorganic components, to achieve synergistic properties. The potential benefits of hydrocarbon fuels that can exist in liquid form under standard temperature and pressure conditions are substantial. The expenses associated with compressing and refrigerating natural gas, coupled with the challenges of swift transportation and storage as a cryogenic liquid, far surpass the costs associated with managing liquid fuels. Oil tankers, which move at a slower pace, can be considered as conduits for transcontinental energy transmission. Through the cooperative regulation of dynamic trajectory and lithiophilic nucleation, the Fe_2CoAl/C host facilitates the uniform deposition of Li-ions. Consequently, the symmetrical cell attains a stable long-term cycling at 1 mA cm^{-2}/1 mA h cm^{-2} for up to 1000 hours. After 900 cycles at 1C, the entire battery using $LiFePO_4$ as the cathode reaches a constant average coulombic efficiency of 99.36%.[49,177] The next generation of high-energy-density Li metal hosts can be made feasible with the help of this synergistic force engineering concept. The investigation of boron nitride nanotubes (BNNTs), a novel tubular material attracting researchers' attention, was prompted by the search for efficient hydrogen storage materials. Experimental results showed that BNNTs were able to store hydrogen more efficiently than CNTs. Due to their tubular structure and point charges, silicon carbide nanotubes (SiCNTs) have also gained attention and are considered potential options for storing hydrogen. The binding energy was found to be 20% higher in theoretical simulations than in pure carbon nanotubes. Another rival in the hydrogen storage market is the carbon nano-scroll (CNS), which is a spiral configuration of carbon-based nanomaterial.[176,179,231] Pure CNSs were unable to store enough hydrogen due to small interlayer distances; however, alkali doping and selective opening produced positive outcomes. The CNS is a spiral configuration of carbon-based nanomaterials and is another competitor in the hydrogen storage space. Small interlayer distances prevented pure CNSs from storing enough hydrogen, although alkali doping and selective opening showed encouraging results. Moreover, SiCNTs have drawn interest and are being evaluated as viable hydrogen storage alternatives because of their tubular structure and point charges.[1,5,9] The anode comprising CNT/SiNPs/SiC exhibited a high specific capacity of 1127.3 mA h g^{-1} at 0.5 A g^{-1} after 200 cycles, corresponding to a remarkable capacity retention of 95.6% (Fig. 16a). However, the anode with CNT/SiNPs/AC or CNT/SiNPs can only supply a capacity of 657.9 mA h g^{-1} and 515.3 mA h g^{-1} at 0.5 A g^{-1} after 200 cycles, respectively. The results indicate that the structure of the inner CNT and the outer SiC, which sandwich the SiNPs, is crucial for the fabrication of a Si-based anode with optimal performance. The active phase for Li^+ storage of the CNT/SiNPs/SiC was evaluated by cyclic CV. As illustrated in Fig. 16b, the peaks observed at 0.18 V in the cathodic scan region can be attributed to the lithiation of crystalline Si into the amorphous Li_xSi alloys (a-Li_xSi). The voltage profiles of CNT/SiNPs/SiC at 2nd, 50th, 100th, 200th cycle demonstrate a smooth progression, with a reduction in polarization as the cycle progresses (Fig. 16c). This indicates the good electrochemical stability of the material. The rate performance of the samples was evaluated by discharge curves at current densities spanning from 0.2 to 4.0 A g^{-1} (Fig. 16d). The CNT/SiNPs/SiC also exhibits a superior lifetime at a large current of 4.0 A g^{-1}, which possesses a high reversible capacity of 745.5 mA h g^{-1} and a capacity retention of 85.5% even after 1000 cycles (Fig. 16e). The lithium-ion diffusion kinetics of materials was investigated by EIS and GITT. The EIS of the CNT/SiNPs/SiC electrode is presented in Fig. 16f. The equivalent circuits employed to fit the EIS data, the values and errors of the electric components are shown in Fig. 16g. The R_{ct} value before the cycle is 73.8 Ω cm^2 and increases to 87.6 Ω cm^2 at the first cycle, which can be attributed to the large polarization effect at the first discharge. However, following the initial cycle, the R_{ct} value exhibits a marked decline as the cycling progresses, reaching a value of 42.8 Ω cm^2 after 100 cycles. This trend was replicated in the parallel test group (Fig. 16h).[1]

4 Fuelling energy *via* modeling, machine learning, and optimization of materials

Materials genome programs and materials informatics have made substantial use of machine learning techniques with massive data created by theory and experiments.[234–238] Experimental data from spectroscopy, imaging, inelastic neutron scattering techniques, *etc.*, have been used in addition to data computed using first-principles theory to speed up the process of designing and discovering new materials. Data from technological advancements have increased the quality and rate of theoretical predictions for the creation of functional materials.[234,238,239] The expense of determining novel structures for unidentified molecules has decreased thanks to machine learning techniques. Moreover, appropriate expectations can be predicted using machine learning techniques, and experimental outcomes can be used to verify the output of the models. The ability of ML to uncover intricate relationships within datasets, optimize material properties, and guide experimental efforts positions it as an indispensable tool at the forefront of materials science research for future energy applications. As researchers delve into the possibilities of new materials to address the evolving challenges of energy sustainability, machine learning stands as a beacon, unlocking novel pathways and accelerating the realization of transformative energy technologies. Moreover, integrating ML with experimental data provides a synergistic approach to materials discovery.[234,240] ML models enhance prediction reliability and applicability by learning from computational simulations and real-world experimental results. This collaborative approach ensures that theoretical advancements in the virtual realm can be seamlessly translated into practical and impactful laboratory developments.

For instance, an assessment was conducted on the pertinent characteristics of TE materials, including heat capacity and thermal conductivity. A combination of qualitative and quantitative techniques based on autonomous workflows and high-

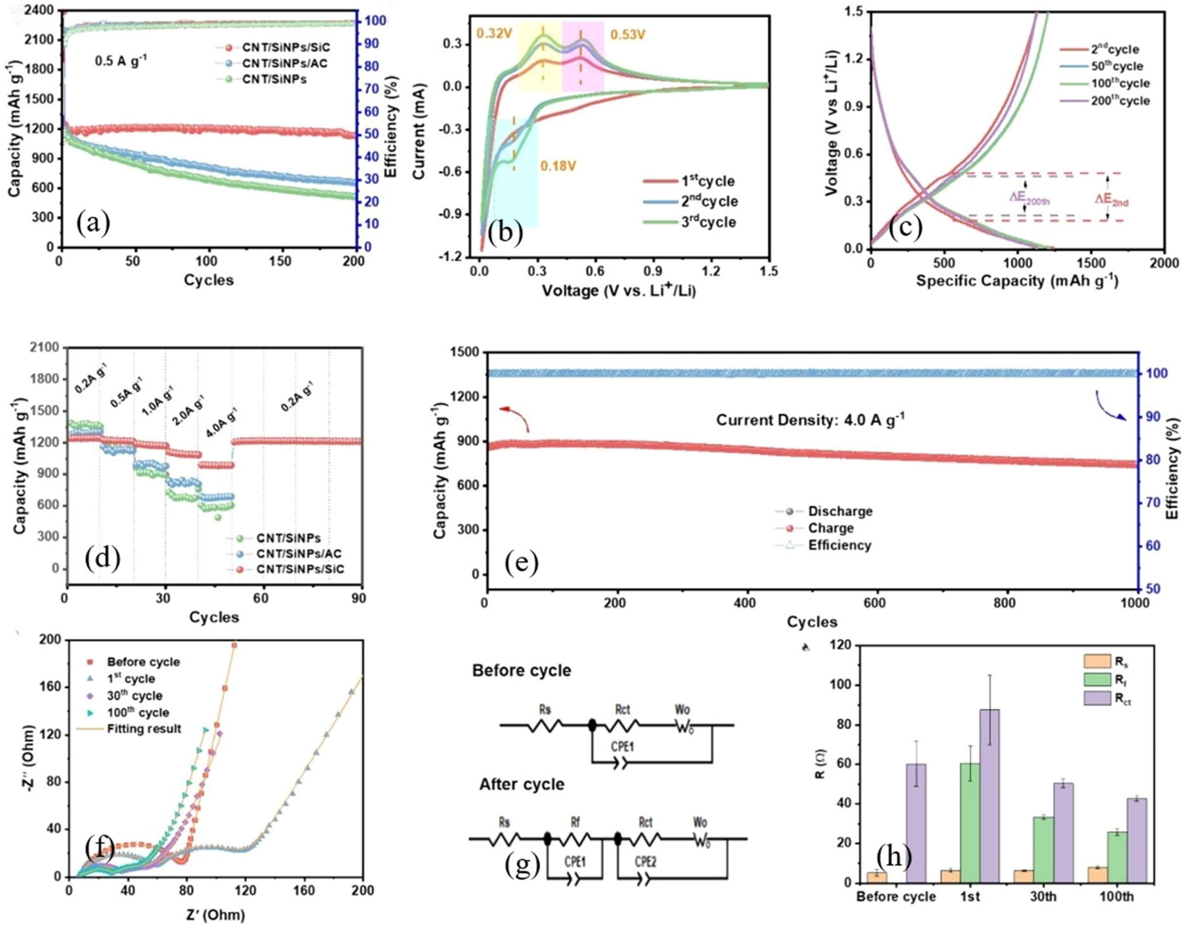

Fig. 16 (a) Cycling-induced variation of discharge capacity and CE for CNT/SiNPs, CNT/SiNPs/AC and CNT/SiNPs/SiC at 0.5 A g^{-1} for 200 cycles. (b) CV curves of CNT/SiNPs/SiC at 0.2 mV s^{-1}. (c) Voltage profiles of CNT/SiNPs/SiC at 0.5 A g^{-1}. (d) Rate capability of CNT/SiNPs, CNT/SiNPs/AC and CNT/SiNPs/SiC at current density of from 0.2 to 4.0 A g^{-1}. (e) Cycling performance of CNT/SiNPs/SiC at 4.0 A g^{-1} for 1000 cycles. (f) Nyquist plots and EIS fitting results of the CNT/SiNPs/SiC electrode before and after cycles and (g) equivalent circuits. (h) Mean and standard deviation of three EIS tests performed on the electrodes. Reproduced with permission.[1–3,232,233] Copyright, 2024. Elsevier.

throughput computations was used to support thermoelectric research on the design, synthesis, and optimization of new materials. There are two types of machine learning tasks: supervised and unsupervised.[24,25,241–243] For labelled data with the desired output value, supervised learning is employed; for data without labels, unsupervised learning is employed. While unsupervised learning looks for patterns in inputs that were previously unknown, supervised learning uses information from training data to create a function that translates an input into an output. Big data analysis has effectively used supervised and unsupervised learning techniques, and these approaches can further the study of TE materials. New knowledge has recently emerged, and several sophisticated materials and informatics tools have been created. Therefore, this is a good moment to give an overview of the most recent developments in this area.[25,241]

When it comes to generating reliable predictions about a compound's qualities, descriptors are important. It can be challenging to choose candidate descriptions when important physics and material features are unclear. Therefore, feature representation is used to characterize the material attributes before model optimization, which often takes a long time.[236,244–246] The time used in selecting descriptors could have been better utilized by researchers to focus on other procedures, such as analysing the model. Thermoelectric research also faces the challenge of selecting descriptors. When it comes to generating reliable predictions about a compound's qualities, descriptors are important. It can be challenging to choose candidate descriptions when important physics and material features are unclear. Therefore, feature representation is used to characterize the material attributes before model optimization, which often takes a long time.[242,243,247] Fig. 17 describes the flow chart of the ML algorithms. Researchers could have better utilized the time used in selecting descriptors to focus on other procedures, such as evaluating the model. Thermoelectric research also faces the challenge of selecting descriptors. Ghiringhelli *et al.* defined the parameters for suitable descriptors, proposed an improved compressed-sensing method, and demonstrated a large feature space by coalescing LASSO and the l0 algorithm.[234] The study indicates that this LASSO-based algorithm contributes to creating

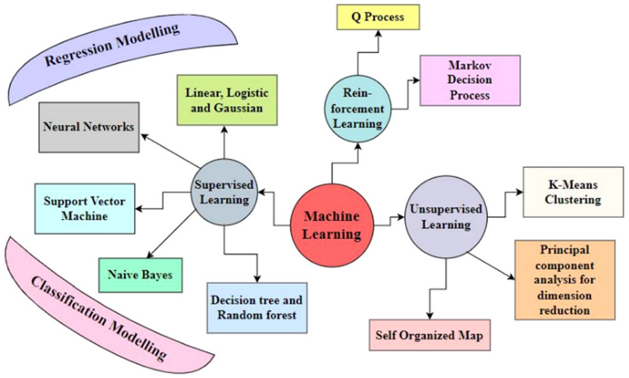

Fig. 17 Flow chart of the ML algorithms.

trustworthy predictions of possible materials. Temperature control is crucial to thermoelectric energy conversion. Van Roekeghem *et al.* identified the 10 most significant components using principal component analysis (PCA) on the force constant data obtained from finite-temperature *ab initio* calculations.[239] After creating a new database with these fundamental elements, they used it to train a regression model. There were found to be 68 stable perovskites. Additionally, it was demonstrated that the thermal conductivity of the cubic perovskites declined more slowly than the temperature's inverse. Carrete *et al.* employed a *k*-means algorithm on a set of half-Heusler compounds data for locating high thermal conductivity at 450 W m K and low thermal conductivity at 23 W m K among the clusters from the screened data.[240] The most significant features of poor conductivity in the clustering were found to be a large average Pauling electronegativity and a low Pettifor scale. With the Boltzmann transport equation and a first-principles simulation, the basic thermoelectric properties may be calculated as exactly as possible in theory. Wang and associates developed an ML model using the ICSD data on the sintered powder samples where a positive Pearson correlation coefficient had been obtained between grain size, electron/hole effective mass and bandgap. To improve the PF and figure of merit *ZT*, the carrier concentration must be optimized.[248] Miller and the group have taken the experimental doped data of semiconductors and predicted the range of carrier concentration using linear regression and compared it with the random forest (RF) model as well as the neural network model.[249] Oliynk and Mar utilized the RF model for identifying structural properties of Heusler compounds with 400 000 data producing an impeccable efficiency and a high degree of accuracy (of about ∼94%).[250] To develop a random-forest model that attempted to predict the crystal structure for any composition, Graser *et al.* trained all the data in Pearson's crystal database. For the structures $CeAl_2Ga_2$, $MgCuAl_2$-type, and $CeNiSi_2$-type, the model's average predicted accuracy was 75% for several high precision levels (over 90%). This method anticipated a broad structural type using machine learning techniques.[235] Similarly, Legrain *et al.* used RF to predict the stability of half-Heusler compounds from *ab initio* computations.[238] Iwasaki *et al.* assessed the thermopower through a temperature gradient, spin current and Seebeck coefficient to obtain a correlation coefficient ∼0.982.[236] However, the underlying physics understanding of the spin-driven Seebeck effect is still unclear; for this reason, the machine learning method can be useful in elucidating previously unidentified correlations. Kolb *et al.* created PROPerty Prophet (PROPhet), a system based on a fully connected neural network, to predict material qualities.[237] In addition to the experimental research, computational explorations of HEMs have been intensifying. Numerous studies using DFT-based computations and *ab initio* molecular simulations (AIMD) to inform material design are now in progress. High-throughput ML-HEA technique was to forecast the ability of solid-solution formation. The *ab initio* and Monte Carlo simulations describe the phase stability and robe short-range order in HEAs. The Materials Project promises to make calculated data on known and projected materials and analytical tools for building novel materials available in the database. However, those computational techniques are not yet suitable for large-scale screening of HEMs because of the disordered solid solution structure, the complexity of the multi-component high entropy systems, and the time-consuming nature of such approaches.[237]

Recently, equilibrium phases have been predicted using CALculation of PHAse Diagrams (CALPHAD) as a direct technique for constructing HEAs. The accuracy of the database is a determining factor in the CALPHAD method's dependability; other multi-component methods remain untested. ML has inherent advantages over traditional modelling and can be used to identify high-entropy systems. High-quality data from many other databases, such as AFLOWLIB, OQMD, and TEDesignLab, have also supported the research. Although there is an increasing need to apply artificial intelligence and machine learning to materials research, the quantity of data available in materials research databases is not as high as in other study fields such as industrial production and image processing. The Bayesian optimization-based method efficiently identified the optimal heterostructure with only a little data.[24,27,87] Fig. 18 shows a pictorial illustration of modelling and optimizing materials for energy.

Since nature-inspired search algorithms are incredibly reliable at resolving intricate issues with several design parameters, they have been significant in electromagnetic design. Additionally, as the subject of metamaterials has advanced, optimization has become important as a means of overcoming performance constraints like high loss and narrow bandwidth, which have prevented metamaterials from being widely used in real-world device applications. Due to their reliable performance, thermoelectric coolers, or TECs, are extensively used to cool several electronic equipment. Two crucial thermoelectric cooler (TEC) performance parameters that can be improved by altering the geometric configuration are cooling capacity and energy efficiency. A thermodynamic model of an exoreversible thermoelectric cooler with a trapezoidal-shaped thermoelectric leg, based on the first and second laws, was created with the Thomson effect taken into account.[245] For a dimensionless cooling load, energy and energy efficiency, figure of merit, and irreversibility, including the Thomson effect, modified equations are determined analytically. Research has been

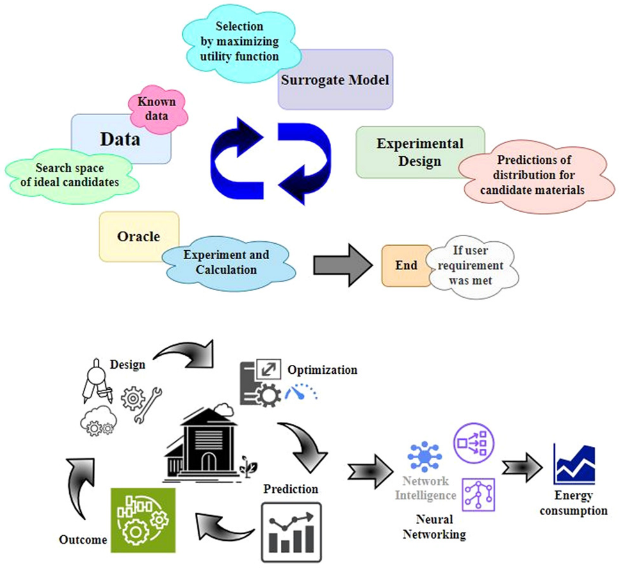

Fig. 18 Pictorial illustration of modelling and optimization of materials for energy.

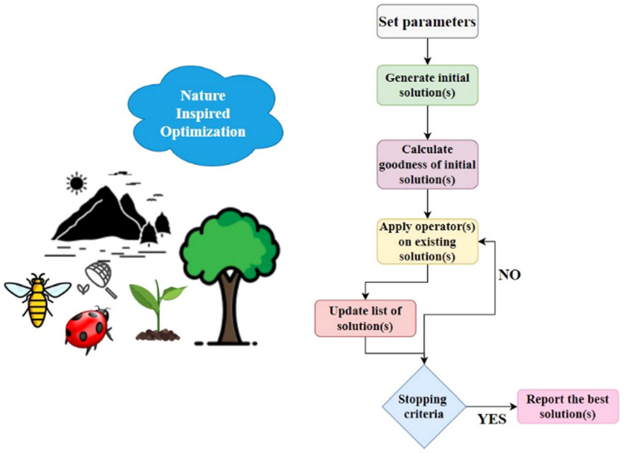

Fig. 19 Flowchart formulated for energy system through nature-inspired optimization algorithm.

conducted on temperature ratio (T_c/T_h) and shape parameter (A_c/A_h) that affect the performance metrics. Second, the genetic algorithm (GA) was used to optimize the cooling capacity and energy efficiency. A novel optimal control method for TEG systems operating in a non-uniform temperature distribution (NUTD) was introduced by Mansoor *et al.* centralized MPPT control has disadvantages due to NUTD on the hot or cold sides of TEG modules, although it can lower the footprint and cost of MPPT of TEG systems and offer superior benefits over cross-tied, string, and distributive control designs.[239] More specifically, in centralized TEG systems, the bypass diodes streamline the power flow, which can result in several local maxima in the electrical characteristics curves of TEG systems. To address these problems, this study presents a unique MPPT control method based on the optimization algorithm equilibrium optimization (EQO), which is based on swarm intelligence (SI). Mirza *et al.* conducted a study on photovoltaic systems that experience substantial power loss because of temperature fluctuations and unpredictable irradiation patterns. Partial shading (PS) is also a significant flaw in the maximum power point tracking (MPPT) controllers that are now in use.[244] This study suggests effective and reliable MPPT controllers for tracking GMPP for various PV array designs using new slime mould optimization (SMO) and improved salp swarm optimization algorithm (ISSA). Refaat and group proposed and investigated a metaheuristic MPPT technique based on an enhanced autonomous group particle swarm optimization algorithm to track GMPP under partial shading conditions.[243] According to the simulation results, the proposed EAGPSO method performs better in terms of fast-tracking time, high acquired power, and high energy efficiency than the equivalent PSO algorithm versions. A series of parallel PV panels arranged in a 3 × 3 array has been used to experimentally validate the EAGPSO approach under PSC. The outcomes of the AGPSO and SPSO algorithms were compared with the EAGPSO algorithm. According to the experimental data, the proposed EAGPSO technique has the lowest power oscillations, at approximately 2.03% of the monitored power with a tracking period of 2.6 s, and the highest MPPT effectiveness of 98.6% among the studied MPPT strategies.[243,246] A flowchart describing the energy-harvesting module obtained from the nature-inspired optimization algorithm is illustrated in Fig. 19.

When comparing renewable energy methods to existing energy sources, the former requires more minerals. According to scenarios provided by the international energy agency (IEA), the demand for raw materials will increase by 30% between 2025 and 2050, with the transportation sector seeing the largest growth. The elements that account for a larger portion of the material requirements for green technologies are aluminium, iron, copper, and potassium. Furthermore, throughout that time, the demand for five elements increased by a factor of at least six: cobalt, lithium, magnesium, titanium, and zinc. This increase is even more pronounced when comparing those results to Greenpeace's AE[R] scenario, which takes a 100% renewable supply into account by 2050. Consequently, eschewing reliance on fossil fuels will mean acknowledging reliance on raw resources.[25,242] Although power plants make up the majority of the material requirements, there is also a significant demand for materials due to grid reinforcement and expansion, which are required to handle significant amounts of unstable power output and provide universal access to electricity. With a 50% chance of keeping global warming at 1.5 °C, GHG emissions from bulk materials (mostly iron/steel and aluminium) might make up a tenth of the remaining carbon budget in the absence of future GHG reduction in the processing industries. However, GHG emissions related to bulk materials in decarbonization pathways won't significantly exceed those in scenarios primarily based on fossil fuels if preference is given to material-efficient technologies, low-carbon processes are implemented in the industries, and increased material recycling is achieved.[241] India's population growth and urbanization will result in a continuous increase in its electrical needs. India has been compelled to switch to renewable energy sources due to climate change, rising carbon emissions, and the depletion of non-renewable energy supplies. If photovoltaic arrays and energy storage infrastructure of a suitable size are installed, India's solar potential is adequate to meet all of its current electrical needs. The dynamics of a photovoltaic power (PV) system as it is constructed to meet all of the world's electricity needs by 2050 were modelled by Sourabh *et al.*[27] The findings demonstrated that it is feasible to construct a photovoltaic system big enough to supply all of the country's electricity needs by 2050, although doing so will need a sharp rise in the installation of solar PV and related storage facilities over the course of the next several decades. Due to the PV system's rapid expansion, a significant amount of electricity will need to be diverted from general societal use and used to construct the solar system's equipment and integrate it with the current infrastructure.

5 Conclusions and future scope

Our capacity to capture and use energy beyond that of humans and animals has changed civilizations and continues to do so. An increasing percentage of people on the planet can travel, communicate over long distances, light their indoor spaces, optimize their temperatures, and fertilize and irrigate their crops, all due to energy production, conversion and storage. Our progressively increased proficiency in locating, extracting, and utilizing energy is the driving force behind this advancement. Materials science research is helping move us closer to a sustainable future that relies on clean energy production, transmission, and distribution, electrical and chemical energy storage, energy efficiency, and improved energy management systems. The mindful use of dependable energy sources is necessary to ensure the sustainability of our near future, given the current technological advancements and improvements. Systems that maximize the planet's energy resources have been developed during the past 30 years, becoming more sophisticated. Unprecedented advancements toward a more technologically sophisticated and sustainable environment include solar cells, piezoelectric and thermoelectric generators, and the ability to obtain hydrogen as an energy vector. Energy autonomy, which is essential for the great majority of gadgets to which we are accustomed, has already been made possible by advancements in energy storage technologies, particularly in the areas of batteries and capacitors. To satisfy expanding needs, such as those in wireless sensor networks and smart control systems for the building sector or heavier industries, the large power per footprint at low-temperature differences is particularly important for micro-scale thermal energy harvesting. We also need to prepare for energy requirements in the technologies coming up soon, such as quantum computing. Upgrading TM generators is anticipated to be able to cover greater areas approaching the meter scale for waste heat recovery without sacrificing the film geometry's ability to transmit heat quickly, and maintaining the condition of resonant self-actuation when placed in parallel architectures. In thermoelectric materials, charge gradients are induced by temperature; it focuses on exploiting thermally induced spin gradients. The class of half-Heuslers offers a simple way to form p- and n-type semiconductors by chemical doping of the parent compound. The alternative way of energetics, *i.e.*, the utility of natural recoverable energy sources based on solar cells, has its realization in wide-gap Heusler insulators. Together with features like shape-memory, electro-chromism, self-healing, photodetection, and thermal response, energy storage and conversion technologies offer a promising area of study with potential applications in biomimetic and artificial intelligence, among other areas. It is possible to achieve challenging improvements in electrochemical performances, such as higher capacitance and better cycling stability, by optimizing the structure or composition. At the same time, practical applications require the optimization of specific functions, which can be accomplished by creating new smart functional materials or by optimizing the nanostructure/composition. There are situations in which improving the electrochemical performance and specific functions is not possible, requiring a balance. These energy devices can also be improvised and made even more appealing to consumers by integrating other novel features like mechanochromism and strain sensing. Meanwhile, theoretical simulation and modelling, along with experimental investigations, are required to unveil the underlying mechanisms to gain deeper and more fundamental knowledge about these intelligent, multipurpose energy devices. In particular, sophisticated *in situ* spectroscopic methods can offer concrete evidence for examining the operation of energy storage and conversion activities. With this development, the research and commercialization of multifunctional energy electronics are expected to accelerate even faster.

Machine learning plays a vital role in advancing the field of energy materials by accelerating the discovery and designing with the development of novel materials with enhanced properties for energy-related applications. ML enables high-throughput screening and data-driven exploration by leveraging algorithms to analyse larger datasets and identify patterns; ML expedites the identification of promising materials with desired properties like conversion efficiency, enhanced thermopower or enriched energy storage. It helps in predicting and optimizing material properties. Once trained on the subject-relevant dataset, the ML models provide quick and nearly accurate predictions of material behaviors, thereby promoting prioritizing and focusing on promising candidates. The synergy between the computational predictions and experimental insights furthers the rendition of theoretical findings into practical applications. ML is especially beneficial in multi-objective optimization, where conflicting material properties must be balanced. In thermoelectric materials, optimizing the electrical conductivity while the minimizing thermal conductivity is a very challenging task. The algorithms can navigate this complex trade-off and guide research problems towards materials with optimized performance for specific energy applications. The necessity for ML in energy materials also arises from the imperative to accelerate the transition to sustainable energy technologies. ML can contribute to the development of materials for efficient catalysis, advanced photovoltaics, next-generation batteries and other critical components of renewable energy systems. By expediting the discovery and optimization of materials with enhanced performance and durability, ML plays a pivotal role in addressing global energy challenges. As the world navigates towards a sustainable energy future, the synergistic convergence of diverse disciplines and innovative technologies will shape the landscape of energy materials, driving progress towards a cleaner, greener and more sustainable universe. By 2050, India's energy production will rely on a mix of conventional and renewable sources, necessitating an array of materials to meet the country's evolving energy needs. Furthermore, measures to improve energy efficiency will rely on materials for efficient appliances, building materials, and clean energy technologies to meet the needs of a rapidly urbanising population. India seeks to enhance energy security and diversify its energy sources; advancements in materials for nuclear power generation and enhanced oil and gas extraction techniques will also be essential. Overall, India's energy transition by 2050 will require diverse energy materials to address its energy security, environmental sustainability, and economic development goals.

Author contributions

A. A. conducted the research and the complete manuscript writing, reviewing and editing. J. P. S. contributed to rewriting and reviewing the manuscript. A. K. contributed to editing the manuscript. N. B. conceptualized and supervised the work.

Data availability

All data generated or analyzed during this study are included in this article.

Conflicts of interest

There are no conflicts to declare.

Acknowledgements

JPS is thankful to Anushandhan National Research Foundation (ANRF) for supporting the work *via* the research grant number RJF/2021/000115.

References

1 F. Di, X. Gu, Y. Chu, L. Li, X. Geng, C. Sun, W. Zhou, H. Zhang, H. Zhao and L. Tao, *J. Colloid Interface Sci.*, 2024, **670**, 204–214.
2 P. De Luna, J. Wei, Y. Bengio, A. Aspuru-Guzik and E. Sargent, *Nature*, 2017, **552**, 23–27.
3 S. Koohi-Fayegh and M. A. Rosen, *J. Energy Storage*, 2020, **27**, 101047.
4 K. Deepak, M. Pattanaik and R. Ramanujan, *Appl. Energy*, 2019, **256**, 113917.
5 Y. Lei, R. Qi, L. Gu, H. Guo, X. Li, Y. Fang, D. Xie, Z. Zheng and Y. Lin, *J. Power Sources*, 2024, **613**, 234902.
6 A. Turabi, H. Karaca, H. Tobe, B. Basaran, Y. Aydogdu and Y. Chumlyakov, *Scr. Mater.*, 2016, **111**, 110–113.
7 Y.-F. Kao, S.-K. Chen, J.-H. Sheu, J.-T. Lin, W.-E. Lin, J.-W. Yeh, S.-J. Lin, T.-H. Liou and C.-W. Wang, *Int. J. Hydrogen Energy*, 2010, **35**, 9046–9059.
8 X. Zang, Y. Jiang, M. Sanghadasa and L. Lin, *Sens. Actuators, A*, 2020, **304**, 111886.
9 P. Vashisth, A. Sharma, M. Nasit, J. P. Singh, M. Varshney, S. Kumar, S. Won and H. Shin, *Heliyon*, 2024, **10**, 15.
10 F. Aversano, M. Palumbo, A. Ferrario, S. Boldrini, C. Fanciulli, M. Baricco and A. Castellero, *Intermetallics*, 2020, **127**, 106988.
11 H.-J. Qiu, G. Fang, J. Gao, Y. Wen, J. Lv, H. Li, G. Xie, X. Liu and S. Sun, *ACS Mater. Lett.*, 2019, **1**, 526–533.
12 H.-J. Qiu, G. Fang, Y. Wen, P. Liu, G. Xie, X. Liu and S. Sun, *J. Mater. Chem. A*, 2019, **7**, 6499–6506.
13 H. Luo, P. Yu, G. Li and K. Yan, *Nat. Rev. Phys.*, 2022, **4**, 611–624.
14 T. M. Gür, *MRS Bull.*, 2021, **46**, 1153–1163.
15 S. Wang, F. Li, G. Zhang and C. Yin, *Energy*, 2023, **267**, 126586.
16 D. Gielen, F. Boshell, D. Saygin, M. D. Bazilian, N. Wagner and R. Gorini, *Energy Strategy Rev.*, 2019, **24**, 38–50.
17 A. Shamoon, A. Haleem, S. Bahl, M. Javaid, C. Prakash and D. Budhhi, *Mater. Today: Proc.*, 2022, **62**, 4260–4266.
18 M. K. Paliwal, S. Jakhar and V. Sharma, *Int. J. Thermofluids*, 2023, **17**, 100310.
19 A. Sharma, V. V. Tyagi, C. R. Chen and D. Buddhi, *Renewable Sustainable Energy Rev.*, 2009, **13**, 318–345.
20 S. Shoeibi, H. Kargarsharifabad, S. A. A. Mirjalily, M. Sadi and A. Arabkoohsar, *J. Energy Storage*, 2022, **50**, 104262.
21 V. Tyagi, K. Chopra, R. Sharma, A. Pandey, S. Tyagi, M. S. Ahmad, A. Sarı and R. Kothari, *Sol. Energy Mater. Sol. Cells*, 2022, **234**, 111392.
22 C. Liu, F. Li, L. P. Ma and H. M. Cheng, *Adv. Mater.*, 2010, **22**, E28–E62.
23 T. M. Gür, *Energy Environ. Sci.*, 2018, **11**, 2696–2767.
24 S. Jain, N. K. Jain and W. J. Vaughn, *Renewable Sustainable Energy Rev.*, 2018, **82**, 1006–1013.
25 G. Kalt, P. Thunshirn, F. Krausmann and H. Haberl, *J. Cleaner Prod.*, 2022, **358**, 132014.
26 C. Chen, Y. Zuo, W. Ye, X. Li, Z. Deng and S. P. Ong, *Adv. Energy Mater.*, 2020, **10**, 1903242.
27 J. Liu, J. G. Zhang, Z. Yang, J. P. Lemmon, C. Imhoff, G. L. Graff, L. Li, J. Hu, C. Wang and J. Xiao, *Adv. Funct. Mater.*, 2013, **23**, 929–946.
28 M. Zäch, C. Hägglund, D. Chakarov and B. Kasemo, *Curr. Opin. Solid State Mater. Sci.*, 2006, **10**, 132–143.
29 Q. Zhang, Y. Sun, W. Xu and D. Zhu, *Adv. Mater.*, 2014, **26**, 6829–6851.

30 M. Massetti, F. Jiao, A. J. Ferguson, D. Zhao, K. Wijeratne, A. Würger, J. L. Blackburn, X. Crispin and S. Fabiano, *Chem. Rev.*, 2021, **121**, 12465–12547.

31 T. Zhu, Y. Liu, C. Fu, J. P. Heremans, J. G. Snyder and X. Zhao, *Adv. Mater.*, 2017, **29**, 1605884.

32 J. He and T. M. Tritt, *Science*, 2017, **357**, eaak9997.

33 L. Yang, Z. G. Chen, M. S. Dargusch and J. Zou, *Adv. Energy Mater.*, 2018, **8**, 1701797.

34 W. Heywang, K. Lubitz, W. Wersing, W. Wersing, W. Heywang, H. Beige and H. Thomann, *Piezoelectricity: Evolution and Future of a Technology*, 2008, pp. 37–87.

35 G. Liu, S. Zhang, W. Jiang and W. Cao, *Mater. Sci. Eng., R*, 2015, **89**, 1–48.

36 P. Jain, A. Stroppa, D. Nabok, A. Marino, A. Rubano, D. Paparo, M. Matsubara, H. Nakotte, M. Fiebig and S. Picozzi, *npj Quantum Mater.*, 2016, **1**, 1–6.

37 A. Bhattad, J. Sarkar and P. Ghosh, *Renewable Sustainable Energy Rev.*, 2018, **82**, 3656–3669.

38 T. M. Koh, H. Wang, Y. F. Ng, A. Bruno, S. Mhaisalkar and N. Mathews, *Adv. Mater.*, 2022, **34**, 2104661.

39 F. Wang, Y. Cao, C. Chen, Q. Chen, X. Wu, X. Li, T. Qin and W. Huang, *Adv. Funct. Mater.*, 2018, **28**, 1803753.

40 Y. Cao, A. Stavrinadis, T. Lasanta, D. So and G. Konstantatos, *Nat. Energy*, 2016, **1**, 1–6.

41 T.-L. Li, Y.-L. Lee and H. Teng, *Energy Environ. Sci.*, 2012, **5**, 5315–5324.

42 R. D. Chavan, M. Wolska-Pietkiewicz, D. Prochowicz, M. Jędrzejewska, M. M. Tavakoli, P. Yadav, C. K. Hong and J. Lewiński, *Adv. Funct. Mater.*, 2022, **32**, 2205909.

43 Z. Tachan, I. Hod, M. Shalom, L. Grinis and A. Zaban, *Phys. Chem. Chem. Phys.*, 2013, **15**, 3841–3845.

44 R. W. Crisp, N. Kirkwood, G. Grimaldi, S. Kinge, L. D. Siebbeles and A. J. Houtepen, *ACS Appl. Energy Mater.*, 2018, **1**, 6569–6576.

45 V. Gupta, N. Chaudhary, R. Srivastava, G. D. Sharma, R. Bhardwaj and S. Chand, *J. Am. Chem. Soc.*, 2011, **133**, 9960–9963.

46 L.-B. Luo, C. Xie, X.-H. Wang, Y.-Q. Yu, C.-Y. Wu, H. Hu, K.-Y. Zhou, X.-W. Zhang and J.-S. Jie, *Nano Energy*, 2014, **9**, 112–120.

47 A. Machín, K. Fontánez, J. C. Arango, D. Ortiz, J. De León, S. Pinilla, V. Nicolosi, F. I. Petrescu, C. Morant and F. Márquez, *Materials*, 2021, **14**, 2609.

48 L. Sun, W. M. Huang, Z. Ding, Y. Zhao, C. C. Wang, H. Purnawali and C. Tang, *Mater. Des.*, 2012, **33**, 577–640.

49 T. Mehtab, G. Yasin, M. Arif, M. Shakeel, R. M. Korai, M. Nadeem, N. Muhammad and X. Lu, *J. Energy Storage*, 2019, **21**, 632–646.

50 P. Qiu, X. Shi and L. Chen, *Energy Storage Mater.*, 2016, **3**, 85–97.

51 S. K. Das and U. Stephen, *Adv. Heat Transfer*, 2009, **41**, 81–197.

52 R. R. Souza, I. M. Gonçalves, R. O. Rodrigues, G. Minas, J. Miranda, A. L. Moreira, R. Lima, G. Coutinho, J. Pereira and A. S. Moita, *Appl. Therm. Eng.*, 2022, **201**, 117725.

53 H. W. Xian, N. A. C. Sidik and G. Najafi, *J. Therm. Anal. Calorim.*, 2019, **135**, 981–1008.

54 T. C. Paul, A. Tikadar, R. Mahamud, A. S. Salman, A. M. Morshed and J. A. Khan, *Processes*, 2021, **9**, 858.

55 C. J. Wort and R. S. Balmer, *Mater. Today*, 2008, **11**, 22–28.

56 J. L. Hudgins, G. S. Simin, E. Santi and M. A. Khan, *IEEE Trans. Power Electron.*, 2003, **18**, 907–914.

57 R. Woods-Robinson, Y. Han, H. Zhang, T. Ablekim, I. Khan, K. A. Persson and A. Zakutayev, *Chem. Rev.*, 2020, **120**, 4007–4055.

58 C. T. Altaf, N. Abdullayeva, N. D. Sankir and N. D. Sankir, *Photoelectrochem. Sol. Cells*, 2018, 251–303.

59 C. Coughlan, *Compound copper chalcogenide nanocrystals: synthetic approaches to fabricate multi-component semiconductor nanocrystals for technological applications*, Doctoral dissertation, University of Limerick, 2014.

60 W. Li, J. M. R. Tan, S. W. Leow, S. Lie, S. Magdassi and L. H. Wong, *Energy Technol.*, 2018, **6**, 46–59.

61 A. Olvera, *Thermoelectric Behavior of Low Thermal Conductivity Cu-based and IV-V Chalcogenides*, Doctoral dissertation, 2017.

62 S. Mandati, P. Misra, B. V. Sarada and T. N. Rao, *Trans. Indian Inst. Met.*, 2019, **72**, 271–288.

63 D. S. Su, W. Neumann and M. Giersig, *Thin Solid Films*, 2000, **361**, 218–222.

64 T. Zhu, C. Fu, H. Xie, Y. Liu and X. Zhao, *Adv. Energy Mater.*, 2015, **5**, 1500588.

65 T. Berry, C. Fu, G. Auffermann, G. H. Fecher, W. Schnelle, F. Serrano-Sanchez, Y. Yue, H. Liang and C. Felser, *Chem. Mater.*, 2017, **29**, 7042–7048.

66 T. Berry, S. Ouardi, G. Fecher, B. Balke, G. Kreiner, G. Auffermann, W. Schnelle and C. Felser, *Phys. Chem. Chem. Phys.*, 2017, **19**, 1543–1550.

67 D. Black, L. Schoensee, J. Richardson, T. Vleisides, N. Kempf, D. Wang, Z. Ren and Y. Zhang, *ACS Appl. Energy Mater.*, 2018, **1**, 5986–5992.

68 F. Casper, T. Graf, S. Chadov, B. Balke and C. Felser, *Semicond. Sci. Technol.*, 2012, **27**, 063001.

69 Z. Zhang, T. Ding, Q. Zhou, Y. Sun, M. Qu, Z. Zeng, Y. Ju, L. Li, K. Wang and F. Chi, *Renewable Sustainable Energy Rev.*, 2021, **148**, 111263.

70 M. M. Rahman, A. O. Oni, E. Gemechu and A. Kumar, *Energy Convers. Manage.*, 2020, **223**, 113295.

71 F. Ren, Z. Wei and X. Zhai, *Renewable Sustainable Energy Rev.*, 2022, **162**, 112440.

72 J. Yang, H. Li, T. Wu, W. Zhang, L. Chen and J. Yang, *Adv. Funct. Mater.*, 2008, **18**, 2880–2888.

73 W. G. Zeier, J. Schmitt, G. Hautier, U. Aydemir, Z. M. Gibbs, C. Felser and G. J. Snyder, *Nat. Rev. Mater.*, 2016, **1**, 1–10.

74 H. Zhu, R. He, J. Mao, Q. Zhu, C. Li, J. Sun, W. Ren, Y. Wang, Z. Liu and Z. Tang, *Nat. Commun.*, 2018, **9**, 2497.

75 Q. Zhang, E. Uchaker, S. L. Candelaria and G. Cao, *Chem. Soc. Rev.*, 2013, **42**, 3127–3171.

76 H. Wang, X. Liang, J. Wang, S. Jiao and D. Xue, *Nanoscale*, 2020, **12**, 14–42.

77 F. Perreault, A. F. De Faria and M. Elimelech, *Chem. Soc. Rev.*, 2015, **44**, 5861–5896.

78 K. Y. Cheong, G. Impellizzeri and M. A. Fraga, *Emerging materials for energy conversion and storage*, Elsevier, 2018.

79 J. Recatala-Gomez, A. Suwardi, I. Nandhakumar, A. Abutaha and K. Hippalgaonkar, *ACS Appl. Energy Mater.*, 2020, **3**, 2240–2257.

80 X.-L. Shi, J. Zou and Z.-G. Chen, *Chem. Rev.*, 2020, **120**, 7399–7515.

81 P. Qiu, X. Huang, X. Chen and L. Chen, *J. Appl. Phys.*, 2009, **106**, 10.

82 L. Wang, L. Miao, Z. Wang, W. Wei, R. Xiong, H. Liu, J. Shi and X. Tang, *J. Appl. Phys.*, 2009, **105**, 1.

83 S. Chen and Z. Ren, *Mater. Today*, 2013, **16**, 387–395.

84 D. Zhao and G. Tan, *Appl. Therm. Eng.*, 2014, **66**, 15–24.

85 J. Wei, L. Yang, Z. Ma, P. Song, M. Zhang, J. Ma, F. Yang and X. Wang, *J. Mater. Sci.*, 2020, **55**, 12642–12704.

86 M. H. Elsheikh, D. A. Shnawah, M. F. M. Sabri, S. B. M. Said, M. H. Hassan, M. B. A. Bashir and M. Mohamad, *Renewable Sustainable Energy Rev.*, 2014, **30**, 337–355.

87 W. Liu, Q. Jie, H. S. Kim and Z. Ren, *Acta Mater.*, 2015, **87**, 357–376.

88 Z. Ma, J. Wei, P. Song, M. Zhang, L. Yang, J. Ma, W. Liu, F. Yang and X. Wang, *Mater. Sci. Semicond. Process.*, 2021, **121**, 105303.

89 M. Gueltig, F. Wendler, H. Ossmer, M. Ohtsuka, H. Miki, T. Takagi and M. Kohl, *Adv. Energy Mater.*, 2017, **7**, 1601879.

90 J. Joseph, M. Ohtsuka, H. Miki and M. Kohl, *Joule*, 2020, **4**, 2718–2732.

91 R. Liu, Y. Xing, J. Liao, X. Xia, C. Wang, C. Zhu, F. Xu, Z.-G. Chen, L. Chen and J. Huang, *Nat. Commun.*, 2022, **13**, 7738.

92 R. J. Quinn and J.-W. G. Bos, *Mater. Adv.*, 2021, **2**, 6246–6266.

93 P. H. Ngan, N. Van Nong, L. T. Hung, B. Balke, L. Han, E. M. J. Hedegaard, S. Linderoth and N. Pryds, *J. Electron. Mater.*, 2016, **45**, 594–601.

94 H. B. Kang, U. Saparamadu, A. Nozariasbmarz, W. Li, H. Zhu, B. Poudel and S. Priya, *ACS Appl. Mater. Interfaces*, 2020, **12**, 36706–36714.

95 L. Fink, S. Kar, K. Lünser, K. Nielsch, H. Reith and S. Fähler, *Adv. Funct. Mater.*, 2023, **33**, 2305273.

96 M. Gueltig, B. Haefner, M. Ohtsuka and M. Kohl, 2013 Transducers & Eurosensors XXVII: The 17th International Conference on Solid-State Sensors, Actuators and Microsystems (TRANSDUCERS & EUROSENSORS XXVII), 2013.

97 T. Kakeshita and T. Fukuda, *Int. J. Appl. Electromagn. Mech.*, 2006, **23**, 45–50.

98 S. Rashidi, M. H. Ehsani, M. Shakouri and N. Karimi, *J. Magn. Magn. Mater.*, 2021, **537**, 168112.

99 S. Pattipaka, J. Jeong, H. Choi, J. Ryu and G.-T. Hwang, *Sensors*, 2022, **22**, 5723.

100 M. Lallart, L. Yan, H. Miki, G. Sebald, G. Diguet, M. Ohtsuka and M. Kohl, *Appl. Energy*, 2021, **288**, 116617.

101 D. Avirovik, R. A. Kishore, D. Vuckovic and S. Priya, *Energy Harvesting Syst.*, 2014, **1**, 13–18.

102 H. Du, Y. Han and L. Wang, *Appl. Phys. A:Mater. Sci. Process.*, 2022, **128**, 555.

103 M. Ujihara, G. P. Carman and D.-G. Lee, *Appl. Phys. Lett.*, 2007, **91**, 9.

104 M. Kohl, M. Gueltig and F. Wendler, *Shape Memory and Superelasticity*, 2018, **vol. 4**, pp. 242–255.

105 F. Z. El Fatnani, D. Guyomar, M. H. Mazroui, F. Belhora and Y. Boughaleb, *Opt. Mater.*, 2016, **56**, 22–26.

106 F. Casadei, T. Delpero, A. Bergamini, P. Ermanni and M. Ruzzene, *J. Appl. Phys.*, 2012, **112**, 6.

107 X. Zhang, Y. Fan, L. Qi and H. Li, *Opt. Mater. Express*, 2016, **6**, 2448–2457.

108 K. Mikoshiba, J. M. Manimala and C. Sun, *J. Intell. Mater. Syst. Struct.*, 2013, **24**, 168–179.

109 L. Griffith, Y. Mudryk, J. Slaughter and V. Pecharsky, *J. Appl. Phys.*, 2018, **123**, 3.

110 L. Mañosa, A. Planes and M. Acet, *J. Mater. Chem. A*, 2013, **1**, 4925–4936.

111 E. Stern-Taulats, P. O. Castillo-Villa, L. Mañosa, C. Frontera, S. Pramanick, S. Majumdar and A. Planes, *J. Appl. Phys.*, 2014, **115**, 17.

112 L. Zhang, J. Zhang, K. Li, L. He, C. Zhou, D. Wang, S. Yang, S. Li and D. Wang, *Acta Mater.*, 2022, **239**, 118245.

113 A. Planes, L. Mañosa, X. Moya, T. Krenke, M. Acet and E. Wassermann, *J. Magn. Magn. Mater.*, 2007, **310**, 2767–2769.

114 J. Y. Law, L. M. Moreno-Ramírez, Á. Díaz-García and V. Franco, *J. Appl. Phys.*, 2023, **133**, 4.

115 A. Berche and P. Jund, *Intermetallics*, 2018, **92**, 62–71.

116 Z. Chen, B. Guo, Y. Yang and C. Cheng, *Phys. B*, 2014, **438**, 1–8.

117 L. T. Govindaraman, A. Arjunan, A. Baroutaji, J. Robinson and A.-G. Olabi, *J. Magn. Magn. Mater.*, 2021, **310**, 2767–2769.

118 Y. Liu and X. Zhang, *Chem. Soc. Rev.*, 2011, **40**, 2494–2507.

119 S. Xiao, T. Wang, T. Liu, C. Zhou, X. Jiang and J. Zhang, *J. Phys. D: Appl. Phys.*, 2020, **53**, 503002.

120 R. S. Kshetrimayum, *IEEE Potentials*, 2004, **23**, 44–46.

121 G. Tatara, H. T. Ueda, K. Taguchi, Y. Sasaki, M. Nishijima and A. Takeuchi, *Phys. Rev. B:Condens. Matter Mater. Phys.*, 2013, **87**, 155102.

122 Y. Ma, Y. Ma, Q. Wang, S. Schweidler, M. Botros, T. Fu, H. Hahn, T. Brezesinski and B. Breitung, *Energy Environ. Sci.*, 2021, **14**, 2883–2905.

123 A. Amiri and R. Shahbazian-Yassar, *J. Mater. Chem. A*, 2021, **9**, 782–823.

124 M. Fu, X. Ma, K. Zhao, X. Li and D. Su, *iScience*, 2021, **24**, 3.

125 N. L. Rosi, J. Eckert, M. Eddaoudi, D. T. Vodak, J. Kim, M. O'Keeffe and O. M. Yaghi, *Science*, 2003, **300**, 1127–1129.

126 M. Sahlberg, D. Karlsson, C. Zlotea and U. Jansson, *Sci. Rep.*, 2016, **6**, 36770.

127 J. Yang, A. Sudik, C. Wolverton and D. J. Siegel, *Chem. Soc. Rev.*, 2010, **39**, 656–675.

128 S.-K. Chen, P.-H. Lee, H. Lee and H.-T. Su, *Mater. Chem. Phys.*, 2018, **210**, 336–347.

129 A. Kitanovski, *Adv. Energy Mater.*, 2020, **10**, 1903741.

130 J. Lyubina, *J. Phys. D: Appl. Phys.*, 2017, **50**, 053002.

131 A. Smith, C. R. Bahl, R. Bjørk, K. Engelbrecht, K. K. Nielsen and N. Pryds, *Adv. Energy Mater.*, 2012, **2**, 1288–1318.

132 B. Shen, J. Sun, F. Hu, H. Zhang and Z. Cheng, *Adv. Mater.*, 2009, **21**, 4545–4564.

133 H. Zhang, R. Gimaev, B. Kovalev, K. Kamilov, V. Zverev and A. Tishin, *Phys. B*, 2019, **558**, 65–73.

134 V. Franco, J. Blázquez, B. Ingale and A. Conde, *Annu. Rev. Mater. Res.*, 2012, **42**, 305–342.

135 V. Franco, J. Blázquez, J. Ipus, J. Law, L. Moreno-Ramírez and A. Conde, *Prog. Mater. Sci.*, 2018, **93**, 112–232.

136 C. Zimm, A. Jastrab, A. Sternberg, V. Pecharsky, K. Gschneidner, M. Osborne and I. Anderson, *Adv. Cryog. Eng.*, 1998, 1759–1766.

137 B. Beckmann, D. Koch, L. Pfeuffer, T. Gottschall, A. Taubel, E. Adabifiroozjaei, O. N. Miroshkina, S. Riegg, T. Niehoff and N. A. Kani, *Acta Mater.*, 2023, **246**, 118695.

138 T. Zilber, S. Cohen, D. Fuks and Y. Gelbstein, *J. Alloys Compd.*, 2019, **781**, 1132–1138.

139 P. K. Kamlesh, R. Agrawal, U. Rani and A. S. Verma, *Mater. Chem. Phys.*, 2022, **275**, 125233.

140 B. A. Bernevig, T. L. Hughes and S.-C. Zhang, *Science*, 2006, **314**, 1757–1761.

141 C. Fu, S. N. Guin, S. J. Watzman, G. Li, E. Liu, N. Kumar, V. Süβ, W. Schnelle, G. Auffermann and C. Shekhar, *Energy Environ. Sci.*, 2018, **11**, 2813–2820.

142 L. Fu and C. L. Kane, *Phys. Rev. B:Condens. Matter Mater. Phys.*, 2007, **76**, 045302.

143 Y. Ma, L. Kou, X. Li, Y. Dai, S. C. Smith and T. Heine, *Phys. Rev. B:Condens. Matter Mater. Phys.*, 2015, **92**, 085427.

144 J. Dong, L. Chen, C. Palmstro/m, R. James and S. McKernan, *Appl. Phys. Lett.*, 1999, **75**, 1443–1445.

145 R. Min, Y. Gao, X. Jiang, X. Yang, L. Li, H. Kang, E. Guo, Z. Chen and T. Wang, *Chem. Eng. J.*, 2023, **464**, 142531.

146 A. Sakai, Y. P. Mizuta, A. A. Nugroho, R. Sihombing, T. Koretsune, M.-T. Suzuki, N. Takemori, R. Ishii, D. Nishio-Hamane and R. Arita, *Nat. Phys.*, 2018, **14**, 1119–1124.

147 H. Reichlova, R. Schlitz, S. Beckert, P. Swekis, A. Markou, Y.-C. Chen, D. Kriegner, S. Fabretti, G. Hyeon Park and A. Niemann, *Appl. Phys. Lett.*, 2018, **113**, 21.

148 L. Li, J. Zeng, W. Qin, P. Cui and Z. Zhang, *Nano Energy*, 2019, **58**, 40–46.

149 Q. Qu, B. Liu, H. Liu, J. Liang, J. Wang, D. Pan and I. K. Sou, *Nanoscale*, 2021, **13**, 18160–18172.

150 C. Shekhar, A. K. Nayak, Y. Sun, M. Schmidt, M. Nicklas, I. Leermakers, U. Zeitler, Y. Skourski, J. Wosnitza and Z. Liu, *Nat. Phys.*, 2015, **11**, 645–649.

151 H. Yang, W. You, J. Wang, J. Huang, C. Xi, X. Xu, C. Cao, M. Tian, Z.-A. Xu and J. Dai, *Phys. Rev. Mater.*, 2020, **4**, 024202.

152 T. Liang, J. Lin, Q. Gibson, T. Gao, M. Hirschberger, M. Liu, R. J. Cava and N. P. Ong, *Phys. Rev. Lett.*, 2017, **118**, 136601.

153 S. Zhou, W. Pei, Y. Zhao, X. Yang, N. Liu and J. Zhao, *npj Comput. Mater.*, 2021, **7**, 186.

154 M. Papaj and L. Fu, *Phys. Rev. B*, 2021, **103**, 075424.

155 M. Yu, G. Li, C. Fu, E. Liu, K. Manna, E. Budiyanto, Q. Yang, C. Felser and H. Tüysüz, *Angew. Chem., Int. Ed.*, 2021, **60**, 5800–5805.

156 P. Yu, W. Fu, Q. Zeng, J. Lin, C. Yan, Z. Lai, B. Tang, K. Suenaga, H. Zhang and Z. Liu, *Adv. Mater.*, 2017, **29**, 1701909.

157 R. Hu, H. Liu, M. Zeng, J. Liu and M. Zhu, *J. Mater. Chem.*, 2012, **22**, 9539–9545.

158 Y. Wang, P. Niu, J. Li, S. Wang and L. Li, *Energy Storage Mater.*, 2021, **34**, 436–460.

159 K. Shi, M. Ren and I. Zhitomirsky, *ACS Sustainable Chem. Eng.*, 2014, **2**, 1289–1298.

160 G. F. I. Toki, M. K. Hossain, W. U. Rehman, R. Z. A. Manj, L. Wang and J. Yang, *Ind. Chem. Mater.*, 2024, 2.

161 D. Lin, Y. Liu and Y. Cui, *Nat. Nanotechnol.*, 2017, **12**, 194–206.

162 G. Yasin, M. Arif, T. Mehtab, X. Lu, D. Yu, N. Muhammad, M. T. Nazir and H. Song, *Energy Storage Mater.*, 2020, **25**, 644–678.

163 D. Yadav, J.-H. Jung, Y. Lee, T. Y.-S. Kim, E. Park, K.-I. Choi, J. Cha, W.-J. Song, J.-H. Choi and S. Doo, *ACS Mater. Lett.*, 2023, **5**, 2648–2655.

164 Y. A. Kumar, N. Roy, T. Ramachandran, M. A. Assiri, S. S. Rao, M. Moniruzzaman and S. W. Joo, *Dalton Trans.*, 2024, **53**, 12410–12433.

165 M. K. Jangid, R. Lakra, V. Srihari, H. K. Poswal, M. Aslam, P. Pant and A. Mukhopadhyay, *ACS Appl. Energy Mater.*, 2019, **2**, 8181–8196.

166 M. Li, K. Fu, Z. Wang, C. Cao, J. Yang, Q. Zhai, Z. Zhou, J. Ji, Y. Xue and C. Tang, *Chem. – Eur. J.*, 2020, **26**, 17567–17573.

167 H. Jung, Y.-U. Kim, M.-S. Sung, Y. Hwa, G. Jeong, G.-B. Kim and H.-J. Sohn, *J. Mater. Chem.*, 2011, **21**, 11213–11216.

168 Y. A. Kumar, S. Vignesh, T. Ramachandran, K. D. Kumar, A. G. Al-Sehemi, M. Moniruzzaman and T. H. Oh, *J. Energy Storage*, 2024, **97**, 112826.

169 Y. A. Kumar, S. Vignesh, T. Ramachandran, A. M. Fouda, H. Hegazy, M. Moniruzzaman and T. H. Oh, *J. Ind. Eng. Chem.*, 2024, **145**.

170 Y. A. Kumar, N. Roy, T. Ramachandran, M. Hussien, M. Moniruzzaman and S. W. Joo, *J. Energy Storage*, 2024, **98**, 113040.

171 Y. Anil Kumar, G. Koyyada, T. Ramachandran, J. H. Kim, S. Sajid, M. Moniruzzaman, S. Alzahmi and I. M. Obaidat, *Nanomaterials*, 2023, **13**, 1049.

172 T. Ramachandran, N. Roy, H. Hegazy, I. Yahia, Y. A. Kumar, M. Moniruzzaman and S. W. Joo, *J. Alloys Compd.*, 2024, 177248.

173 Y. A. Kumar, J. K. Alagarasan, T. Ramachandran, M. D. Rezeq, M. A. Bajaber, A. A. Alalwiat, M. Moniruzzaman and M. Lee, *J. Energy Storage*, 2024, **86**, 111119.

174 J. Yan, S. Li, B. Lan, Y. Wu and P. S. Lee, *Adv. Funct. Mater.*, 2020, **30**, 1902564.

175 N. Choudhary, S. Singh, S. Bhardwaj, S. Gupta, U. Nandi, R. Chandra and P. K. Maji, *Carbohydr. Polym. Technol. Appl.*, 2023, 100416.

176 Z. Yang, J. Tian, Z. Yin, C. Cui, W. Qian and F. Wei, *Carbon*, 2019, **141**, 467–480.

177 I. Karbhal, V. Chaturvedi, P. Yadav, A. Patrike and M. V. Shelke, *Adv. Mater. Interfaces*, 2023, **10**, 2201560.

178 A. Eftekhari, L. Li and Y. Yang, *J. Power Sources*, 2017, **347**, 86–107.

179 C. Zhi, Y. Bando, C. Tang and D. Golberg, *Mater. Sci. Eng., R*, 2010, **70**, 92–111.

180 S. Kumar, M. Nehra, D. Kedia, N. Dilbaghi, K. Tankeshwar and K.-H. Kim, *Prog. Energy Combust. Sci.*, 2018, **64**, 219–253.

181 S. Shen, Y. Chen, J. Zhou, H. Zhang, X. Xia, Y. Yang, Y. Zhang, A. Noori, M. F. Mousavi and M. Chen, *Adv. Energy Mater.*, 2023, **13**, 2204259.

182 Y. Kato, S. Hori and R. Kanno, *Adv. Energy Mater.*, 2020, **10**, 2002153.

183 Y. Nikodimos, W. N. Su and B. J. Hwang, *Adv. Energy Mater.*, 2023, **13**, 2202854.

184 A. J. Samson, K. Hofstetter, S. Bag and V. Thangadurai, *Energy Environ. Sci.*, 2019, **12**, 2957–2975.

185 M. Abreu-Sepúlveda, D. E. Williams, A. Huq, C. Dhital, Y. Li, M. P. Paranthaman, K. Zaghib and A. Manivannan, *Ionics*, 2016, **22**, 317–325.

186 C. Chen, K. Wang, H. He, E. Hanc, M. Kotobuki and L. Lu, *Small*, 2023, **19**, 2205550.

187 M. Xue, W. Lu, S. Xue and C. Zhang, *J. Mater. Sci.*, 2021, **56**, 19614–19622.

188 X. Feng, L. Zhang, C. Li, M. Shen, R. Zheng, Z. Wang, H. Sun and Y. Liu, *Ceram. Int.*, 2024, **50**, 38999–39009.

189 E. Cha, J. H. Yun, R. Ponraj and D. K. Kim, *Mater. Chem. Front.*, 2021, **5**, 6294–6314.

190 Z. W. Seh, Y. Sun, Q. Zhang and Y. Cui, *Chem. Soc. Rev.*, 2016, **45**, 5605–5634.

191 J. Chen, M. Fang, Q. Wu, S. Tang, J. Zheng, C. Wei, X. Cao, Y. Shi, N. Xu and Y. He, *Chem. Mater.*, 2025, DOI: **10.1021/acs.chemmater.4c01152**.

192 A. G. Paul-Orecchio, L. Stockton, J. A. Weeks, A. Dolocan, Y. Wang and C. B. Mullins, *ACS Energy Lett.*, 2023, **8**, 4228–4234.

193 J. Yi, S. Guo, P. He and H. Zhou, *Energy Environ. Sci.*, 2017, **10**, 860–884.

194 M. F. Gaele and T. M. Di Palma, *Energy Fuels*, 2022, **36**, 12875–12895.

195 A. Liu, S. Lu and X. Wu, *Batteries Supercaps*, 2024, **7**, e202400290.

196 T. Jin, H. Li, K. Zhu, P.-F. Wang, P. Liu and L. Jiao, *Chem. Soc. Rev.*, 2020, **49**, 2342–2377.

197 J. W. Suen, N. K. Elumalai, S. Debnath, N. M. Mubarak, C. I. Lim and M. M. Reddy, *Adv. Mater. Interfaces*, 2022, **9**, 2201405.

198 S. R. Mangishetti, D. Jang, J. Choi, G. Rajeshkhanna, S. Pittala, S. K. Kang, J. Ji, M. Kim, S. G. Jung and J. Ha, *Chem. Eng. J.*, 2023, **472**, 144863.

199 S. Venkateshwaran, K. Selvakumar, V. Duraisamy and S. M. S. Kumar, *Photocatalysts-New Perspectives*, IntechOpen, 2023.

200 J. H. Lee, G. Ali, D. H. Kim and K. Y. Chung, *Adv. Energy Mater.*, 2017, **7**, 1601491.

201 J. Ge, L. Fan, A. M. Rao, J. Zhou and B. Lu, *Nat. Sustainability*, 2022, **5**, 225–234.

202 B. Ahmed, A. E. Ghazaly and J. Rosen, *Adv. Funct. Mater.*, 2020, **30**, 2000894.

203 K. H. Lee, Y.-Z. Zhang, Q. Jiang, H. Kim, A. A. Alkenawi and H. N. Alshareef, *ACS Nano*, 2020, **14**, 3199–3207.

204 R. Li, L. Zhang, L. Shi and P. Wang, *ACS Nano*, 2017, **11**, 3752–3759.

205 Z. W. Seh, K. D. Fredrickson, B. Anasori, J. Kibsgaard, A. L. Strickler, M. R. Lukatskaya, Y. Gogotsi, T. F. Jaramillo and A. Vojvodic, *ACS Energy Lett.*, 2016, **1**, 589–594.

206 L. Ding, D. Xiao, Z. Lu, J. Deng, Y. Wei, J. Caro and H. Wang, *Angew. Chem.*, 2020, **132**, 8798–8804.

207 Y. Dong, S. S. K. Mallineni, K. Maleski, H. Behlow, V. N. Mochalin, A. M. Rao, Y. Gogotsi and R. Podila, *Nano Energy*, 2018, **44**, 103–110.

208 G. Gao, A. P. O'Mullane and A. Du, *ACS Catal.*, 2017, **7**, 494–500.

209 A. Mankuni and S. Varghese, *ACS Appl. Electron. Mater.*, 2024, **6**, 4194–4203.

210 V. A. Cao, M. Kim, S. Lee, C. G. Kim, P. Cao Van, T. N. Thi, J.-R. Jeong and J. Nah, *ACS Appl. Mater. Interfaces*, 2022, **14**, 26824–26832.

211 Y.-Y. Peng, B. Akuzum, N. Kurra, M.-Q. Zhao, M. Alhabeb, B. Anasori, E. C. Kumbur, H. N. Alshareef, M.-D. Ger and Y. Gogotsi, *Energy Environ. Sci.*, 2016, **9**, 2847–2854.

212 Q. Jiang, N. Kurra, K. Maleski, Y. Lei, H. Liang, Y. Zhang, Y. Gogotsi and H. N. Alshareef, *Adv. Energy Mater.*, 2019, **9**, 1901061.

213 Z. Zhang, S. Yang, P. Zhang, J. Zhang, G. Chen and X. Feng, *Nat. Commun.*, 2019, **10**, 2920.

214 M. Salauddin, S. S. Rana, M. Sharifuzzaman, M. T. Rahman, C. Park, H. Cho, P. Maharjan, T. Bhatta and J. Y. Park, *Adv. Energy Mater.*, 2021, **11**, 2002832.

215 S. Li, C. Yu, J. Yang, C. Zhao, M. Zhang, H. Huang, Z. Liu, W. Guo and J. Qiu, *Energy Environ. Sci.*, 2017, **10**, 1958–1965.

216 Y. Yang, H. Deng and Q. Fu, *Mater. Chem. Front.*, 2020, **4**, 3130–3152.

217 V. M. H. Ng, H. Huang, K. Zhou, P. S. Lee, W. Que, J. Z. Xu and L. B. Kong, *J. Mater. Chem. A*, 2017, **5**, 3039–3068.

218 J. S. Won, C. Prasad, S.-G. Jeong, P. Rosaiah, A. S. Reddy, Z. Ahmad, S. Sangaraju and H. Y. Choi, *Int. J. Biol. Macromol.*, 2023, **240**, 124477.

219 C. J. Zhang, L. McKeon, M. P. Kremer, S.-H. Park, O. Ronan, A. Seral-Ascaso, S. Barwich, C. Ó. Coileáin, N. McEvoy and H. C. Nerl, *MXenes*, Jenny Stanford Publishing, 2023, pp. 463–485.

220 S. Sarikurt, D. Çakır, M. Keçeli and C. Sevik, *Nanoscale*, 2018, **10**, 8859–8868.

221 Y. Wei, Z. Zhou, J. Liu, B. Zhang, G. Wang, G. Han, G. Wang, X. Zhou and X. Lu, *Acta Mater.*, 2022, **241**, 118369.

222 S. Saharan, U. Ghanekar and S. Meena, *J. Phys. Chem. C*, 2023, **127**, 8905–8912.

223 K. Liang, T. Wu, S. Misra, C. Dun, S. Husmann, K. Prenger, J. J. Urban, V. Presser, R. R. Unocic and D. E. Jiang, *Adv. Sci.*, 2024, **11**, 2402708.

224 K. Namsheer and C. S. Rout, *RSC Adv.*, 2021, **11**, 5659–5697.

225 Y. Zhao, Z. Song, X. Li, Q. Sun, N. Cheng, S. Lawes and X. Sun, *Energy Storage Mater.*, 2016, **2**, 35–62.

226 Q. Du, R. Rao, F. Bi, Y. Yang, W. Zhang, Y. Yang, N. Liu and X. Zhang, *Surf. Interfaces*, 2022, **28**, 101647.

227 Y. Fang, Z. Yang, H. Li and X. Liu, *Environ. Sci. Pollut. Res.*, 2020, **27**, 4703–4724.

228 A. Jana, S. Bähring, M. Ishida, S. Goeb, D. Canevet, M. Sallé, J. O. Jeppesen and J. L. Sessler, *Chem. Soc. Rev.*, 2018, **47**, 5614–5645.

229 S. M. Sajjadinezhad, L. Boivin, K. Bouarab and P. D. Harvey, *Coord. Chem. Rev.*, 2024, **510**, 215794.

230 Z. Qian, R. Zhang, Y. Xiao, H. Huang, Y. Sun, Y. Chen, T. Ma and X. Sun, *Adv. Energy Mater.*, 2023, **13**, 2300086.

231 A. Kashyout, H. M. Soliman, M. Fathy, E. Gomaa and A. A. Zidan, *Int. J. Photoenergy*, 2012, **2012**, 952610.

232 H. Jeong, Y. H. Kim, B.-R. Won, H. Jeon, C.-H. Park and J.-H. Myung, *Chem. Mater.*, 2023, **35**, 3745–3764.

233 A. G. Olabi, Q. Abbas, P. A. Shinde and M. A. Abdelkareem, *Energy*, 2023, **266**, 126408.

234 L. M. Ghiringhelli, J. Vybiral, S. V. Levchenko, C. Draxl and M. Scheffler, *Phys. Rev. Lett.*, 2015, **114**, 105503.

235 J. Graser, S. K. Kauwe and T. D. Sparks, *Chem. Mater.*, 2018, **30**, 3601–3612.

236 Y. Iwasaki, I. Takeuchi, V. Stanev, A. G. Kusne, M. Ishida, A. Kirihara, K. Ihara, R. Sawada, K. Terashima and H. Someya, *Sci. Rep.*, 2019, **9**, 2751.

237 B. Kolb, L. C. Lentz and A. M. Kolpak, *Sci. Rep.*, 2017, **7**, 1192.

238 F. Legrain, J. Carrete, A. Van Roekeghem, G. K. Madsen and N. Mingo, *J. Phys. Chem. B*, 2018, **122**, 625–632.

239 A. van Roekeghem, J. Carrete, C. Oses, S. Curtarolo and N. Mingo, *Phys. Rev. X*, 2016, **6**, 041061.

240 J. Carrete, W. Li, N. Mingo, S. Wang and S. Curtarolo, *Phys. Rev. X*, 2014, **4**, 011019.

241 S. Bhattacharya, R. Banerjee, V. Ramadesigan, A. Liebman and R. Dargaville, 2023 North American Power Symposium (NAPS), 2023.

242 A. Das, V. Saini, K. Parikh, J. Parikh, P. Ghosh and M. Tot, *Energy Strategy Rev.*, 2023, **45**, 101042.

243 A. Refaat, A.-E. Khalifa, M. M. Elsakka, Y. Elhenawy, A. Kalas and M. H. Elfar, *Energy Convers. Manage.*, 2023, **287**, 117124.

244 M. Mansoor, A. F. Mirza, S. Duan, J. Zhu, B. Yin and Q. Ling, *Energy Convers. Manage.*, 2021, **246**, 114694.

245 D. H. Werner, J. A. Bossard, Z. Bayraktar, Z. H. Jiang, M. D. Gregory and P. L. Werner, *Numerical Methods for Metamaterial Design*, 2013, pp. 97–146.

246 A. F. Mirza, M. Mansoor, K. Zhan and Q. Ling, *Energy*, 2021, **228**, 120602.

247 R. Lamba, S. Manikandan, S. Kaushik and S. Tyagi, *Therm. Sci. Eng. Prog.*, 2018, **6**, 236–250.

248 Z. L. Wang, Y. Yokoyama, T. Onda, Y. Adachi and Z. C. Chen, *Adv. Electron. Mater.*, 2019, **5**, 1900079.

249 S. A. Miller, M. Dylla, S. Anand, K. Gordiz, G. J. Snyder and E. S. Toberer, *npj Comput. Mater.*, 2018, **4**, 71.

250 A. O. Oliynyk and A. Mar, *Acc. Chem. Res.*, 2018, **51**, 59–68.